Extension of the Particle X-ray Coincidence Technique (PXCT) to Astrophysical Reaction Rates

L. J. Sun[1],* J. Dopfer[2,1], A. Adams[2,1], C. Wrede[2,1],† A. Banerjee[3,4], B. A. Brown[2,1], R. Mahajan[1], T. Rauscher[5,6], C. Sumithrarachchi[1], D. Weisshaar[1], and T. Wheeler[2,1,7]

[1] *Facility for Rare Isotope Beams, Michigan State University, East Lansing, Michigan 48824, USA*
[2] *Department of Physics and Astronomy, Michigan State University, East Lansing, Michigan 48824, USA*
[3] *GSI Helmholtzzentrum für Schwerionenforschung GmbH, Darmstadt 64291, Germany*
[4] *Saha Institute of Nuclear Physics, Kolkata, West Bengal 700064, India*
[5] *Department of Physics, University of Basel, 4056 Basel, Switzerland*
[6] *Centre for Astrophysics Research, University of Hertfordshire, Hatfield AL10 9AB, UK*
[7] *Department of Computational Mathematics, Science, and Engineering, Michigan State University, East Lansing, Michigan 48824, USA*

(Dated: September 5, 2024)

The Particle X-ray Coincidence Technique (PXCT) was originally developed to measure average lifetimes in the $10^{-17} - 10^{-15}$ s range for proton-unbound states populated by electron capture (EC). We have designed and built a detection system in the stopped-beam area at the Facility for Rare Isotope Beams that extends PXCT to measure both lifetimes and decay branching ratios of resonances populated by EC/β^+ decay. The first application of this system aims to obtain essential nuclear data from ^{60}Ga EC/β^+ decay to constrain the thermonuclear rates of the ^{59}Cu$(p,\gamma)^{60}$Zn and ^{59}Cu$(p,\alpha)^{56}$Ni reactions, and in turn, the strength of the NiCu cycle, which is predicted to significantly impact the modeling of Type I X-ray burst light curves and the composition of the burst ashes. Detailed theoretical calculations, Monte Carlo simulations, and performance tests with radioactive sources have been conducted to validate the feasibility of employing the PXCT system for the ^{60}Ga experiment. PXCT serves as a powerful platform to measure nearly all essential parameters for thermonuclear reaction rate calculations in a single experiment, potentially improving the accuracy and consistency of astrophysically relevant nuclear inputs.

I. INTRODUCTION

Direct measurements of charged-particle thermonuclear reaction rates represent a major challenge due to the small cross-section at stellar energies and technical challenges associated with beam intensity limitations, target degradation under bombardment, and low signal-to-background ratios. Successful direct measurements at astrophysical energies have been achieved only in a few instances [1]. Consequently, direct measurements of thermonuclear reaction rates often have to be performed at higher energies and then extrapolated down to stellar energies with the aid of nuclear theory. Alternatively, various indirect approaches, such as elastic scattering, transfer reactions, surrogate reactions, charge-exchange reactions, Coulomb dissociation, in-beam γ-ray spectroscopy, β-decay spectroscopy have also played a major role in a comprehensive understanding of thermonuclear reactions [2–4]. However, these methods typically yield only a fraction of the necessary nuclear data, and results from multiple experiments still need to be pieced together to piece together to infer the reaction rates of interest [5].

The thermonuclear charged-particle reactions are often dominated by narrow and isolated resonances if the level density of the compound nucleus in the Gamow window is not too high. The resonant reaction rate can be calculated using the well-known expression [6, 7]:

$$N_A\langle\sigma\nu\rangle_r = 1.5394\times10^{11}(\mu T_9)^{-3/2}\times\omega\gamma \times\exp\left(-\frac{11.605E_r}{T_9}\right)(\mathrm{cm^3 s^{-1} mol^{-1}}), \quad (1)$$

where $\mu = A_pA_T/(A_p+A_T)$ is the reduced mass in atomic mass units, with A_p and A_T as the mass numbers of the incoming particle and the target nucleus, respectively. E_r is the resonance energy in the center-of-mass system in units of MeV. T_9 is the temperature in units of giga kelvin (GK), and $\omega\gamma$ is the resonance strength in units of MeV. For a (p,γ) resonance,

$$\omega\gamma = \frac{2J_r+1}{(2J_p+1)(2J_T+1)}\frac{\Gamma_p\Gamma_\gamma}{\Gamma_{\mathrm{tot}}}, \quad (2)$$

where J_r is the spin of the resonance, $J_p = 1/2$ is the spin of proton, and J_T is the spin of the ground state of the target nucleus. The total decay width Γ_{tot} of the resonance is the sum of the partial widths for open decay channels, typically including proton width (Γ_p), γ width (Γ_γ), and α width (Γ_α). Equivalently, the resonance strength can be constructed by combining the proton branching ratio $B_p = \Gamma_p/\Gamma_{\mathrm{tot}}$, the γ-ray branching ratio $B_\gamma = \Gamma_\gamma/\Gamma_{\mathrm{tot}}$, and the lifetime τ using the following expression:

* sunli@frib.msu.edu
† wrede@frib.msu.edu

$$\omega\gamma = \frac{2J_r+1}{(2J_p+1)(2J_T+1)} B_p B_\gamma \frac{\hbar}{\tau}, \quad (3)$$

where $\hbar$ is the reduced Planck constant. These relations are also applicable to a (p,α) resonance by replacing the terms Γ_γ and B_γ with Γ_α and B_α, respectively. Therefore, important quantities to determine the reaction rates include the resonance energies, the spins, the proton, γ-ray, and α-decay branching ratios, and the lifetimes of the resonances.

Suppose the level density of resonances in the compound nucleus is sufficiently high to justify a statistical treatment, a (p,γ) reaction cross-section can be estimated within the Hauser-Feshbach statistical model framework:

$$\sigma_{p\gamma} = \frac{\pi\hbar^2}{2\mu E_r (2J_p+1)(2J_T+1)} \sum_{J,\pi} (2J+1) \frac{T_p^{J^\pi} T_\gamma^{J^\pi}}{\sum_k T_k^{J^\pi}}, \quad (4)$$

where μ is the reduced mass, E_r, J, and π are the energy, spin, and parity of the resonance in the compound nucleus, J_p and J_T are the spins of the proton and the state in the target nucleus, respectively. $T_p^{J^\pi}$ and $T_\gamma^{J^\pi}$ are the transmission coefficients for the proton and γ channels, respectively, of the resonance. $\sum_k T_k^{J^\pi}$ represents the sum of the transmission coefficients over all possible decay channels k of the resonance, including proton, α, and γ channels. Both particle and γ transmission coefficients are related to partial widths and level densities. The important inputs for statistical model calculations are the particle and γ transmission coefficients and the level densities of excited states in the compound nucleus [8, 9].

In this paper, we introduce a detection system that applies the Particle X-ray Coincidence Technique [10] to measure practically all essential parameters for thermonuclear reaction rate calculations in a single experiment, potentially improving the accuracy and consistency of astrophysically relevant nuclear inputs. We demonstrate the feasibility of this technique through a case study focusing on the NiCu cycle issue in Type I X-ray bursts (XRBs) and provide a detailed description of the experimental setup and its performance tests.

II. CASE STUDY: NICU CYCLE IN XRBS

Type I XRBs are the most frequent type of thermonuclear stellar explosions in the Galaxy. They are powered by thermonuclear runaways in hydrogen- and/or helium-rich material accreted onto the surface of a neutron star in a low-mass X-ray binary system. The main nuclear reaction flow in the XRB is driven towards the proton drip line and to higher masses via a series of particle-induced reactions and β^+-decays. Accurate modeling of energy production and nucleosynthesis in XRBs requires precise nuclear physics inputs, including β decay rates, nuclear masses, and nuclear reaction rates of proton-rich rare isotopes along the path of the rapid proton (rp) capture process. Our understanding of XRBs has greatly expanded, yet many open questions still remain despite decades of work [11–13].

As illustrated in Fig. 1, under XRB conditions, the rp-process beyond the waiting point ^{56}Ni may be affected by several cycles, such as the NiCu cycle and ZnGa cycle one α cluster above. The strength of the cycles is determined by the ratio of the (p,α) to (p,γ) reaction rates at ^{59}Cu and ^{63}Ga, respectively. A low ^{59}Cu$(p,\gamma)^{60}$Zn rate or a high ^{59}Cu$(p,\alpha)^{56}$Ni rate would lead to the formation of a NiCu cycle, returning the reaction flux to ^{56}Ni, strongly impeding the synthesis of heavier nuclei and affecting the XRB observables [14]. Currently, both rates recommended by REACLIB [15] are calculated by the Hauser-Feshbach statistical model [8, 16]. The variations in these rates have been identified as having a significant impact on the modeling of XRB light curves and the composition of the burst ashes [17–19]. The competition between ^{59}Cu$(p,\gamma)^{60}$Zn and ^{59}Cu$(p,\alpha)^{56}$Ni reactions at higher temperatures (~3 GK) is found to have a significant impact on the νp-process nucleosynthesis in core-collapse supernovae [20–22].

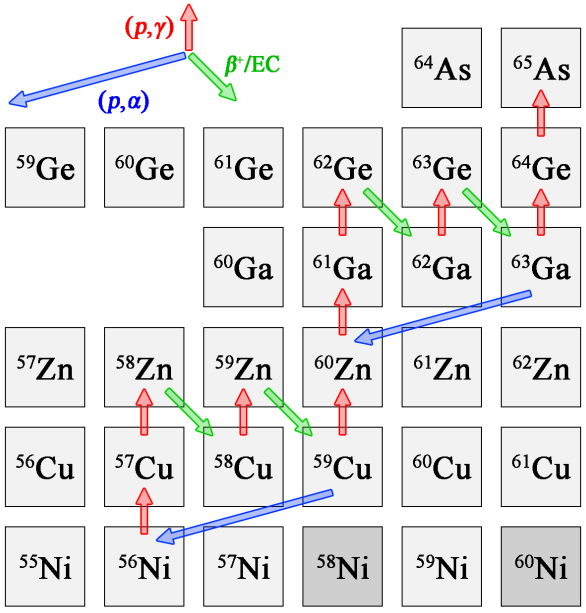

FIG. 1. Portion of the rp-process reaction sequence featuring the NiCu and ZnGa cycles. ^{58}Ni and ^{60}Ni are stable.

It is not currently possible to directly measure these two reactions at astrophysical energies because the predicted cross sections are too small, and intense low-energy radioactive ^{59}Cu beams are not available. A ^{59}Cu$(p,\alpha)^{56}$Ni reaction measurement using a ^{59}Cu beam with an intensity of 3600 particle per second

(pps) and a cryogenic solid H_2 target at center-of-mass energy $E_{\rm c.m.} = 6.0$ MeV found that ^{59}Cu(p,α) proceeds predominantly to ^{56}Ni ground state, and standard statistical model calculations overestimate the cross section by a factor of 1.6−4 [23]. In a ^{58}Ni$(^3$He$,n)^{60}$Zn reaction measurement [24], the nuclear level density of ^{60}Zn was extracted from the neutron evaporation spectrum. At an excitation energy of 6 MeV, the level density is estimated to be ∼18 MeV^{-1}. Taking into account the spin and parity range relevant to $\ell = 0, 1$ proton captures (Table I), the level density could be lower than the applicability of the Hauser-Feshbach statistical model. Kim *et al.* [25] evaluated available experimental data on ^{60}Zn resonances, supplemented with theoretical calculations. They found the ^{59}Cu$(p,\alpha)^{56}$Ni reaction rate to be lower than the REACLIB rate [15] at XRB temperatures, implying a weaker NiCu cycle strength than previously estimated [17–19].

There are several ongoing efforts to address this problem both directly and indirectly, such as the ^{56}Ni$(\alpha,p)^{59}$Cu reaction measurement using 2.25, 2.40, and 2.65-MeV/nucleon ^{56}Ni beam of 3000 pps on a He jet target with the Jet Experiments in Nuclear Structure and Astrophysics setup [26], ^{59}Cu$(p,\alpha)^{56}$Ni reaction measurement using an 8.4-MeV/nucleon ^{59}Cu beam with the Multi-Sampling Ionization Chamber [27], ^{60}Zn γ-ray spectroscopy via the ^{59}Cu$(d,n)^{60}$Zn transfer reaction using Gamma-Ray Energy Tracking In-beam Nuclear Array [28], ^{60}Ga β-delayed γ decay total absorption spectroscopy using the Summing NaI detector [29], and ^{60}Ga decay using the Gaseous Detector with Germanium Tagging [30]. To this day, experimental constraints on the ^{59}Cu$(p,\gamma)^{60}$Zn and ^{59}Cu$(p,\alpha)^{56}$Ni are still scarce and preclude a robust understanding of their astrophysical impacts.

Table I summarizes the spins and parities of relevant ^{60}Zn resonances. It is evident that only positive parity states associated with $\ell = 1$ proton captures are accessible via allowed ^{60}Ga β transitions, also indicating that a lower density of levels populated in the β decay than in the previous ^{58}Ni$(^3$He$,n)^{60}$Zn reaction measurement [24].

TABLE I. Properties of ^{60}Zn states populated via proton captures on the $3/2^-$ ^{59}Cu ground state and the $1/2^-$ ^{59}Cu first excited state, and the allowed β transitions of the 2^+ ^{60}Ga ground state.

Population	^{60}Zn states
$\ell = 0$ p on $3/2^-$	1^-, 2^-
$\ell = 1$ p on $3/2^-$	0^+, 1^+, 2^+, 3^+
$\ell = 2$ p on $3/2^-$	0^-, 1^-, 2^-, 3^-, 4^-
$\ell = 0$ p on $1/2^-$	0^-, 1^-
$\ell = 1$ p on $1/2^-$	0^+, 1^+, 2^+
$\ell = 2$ p on $1/2^-$	1^-, 2^-, 3^-
β from 2^+	1^+, 2^+, 3^+

The Gamow energies and windows for the ^{59}Cu$(p,\gamma)^{60}$Zn and ^{59}Cu$(p,\alpha)^{56}$Ni reactions shown in Table II are calculated from a numerical study of the relevant energy ranges for astrophysical reaction rates [31]. Discussing these two reactions at temperatures below 0.5 GK is not relevant as the abundance flow cannot reach this mass region [7, 14]. Combined with the proton-separation energy of ^{60}Zn $S_p(^{60}\text{Zn}) = 5105.0(4)$ keV [32] and α-separation energy of ^{60}Zn $S_\alpha(^{60}\text{Zn}) = 2691.7(5)$ keV [32], ^{60}Zn resonances of interest are energetically accessible in ^{60}Ga β decay owing to the large $Q_{\rm EC}(^{60}\text{Ga}) = 14161(15)$ keV [33, 34].

Fig. 2 summarizes currently known ^{60}Ga decay properties. Mazzocchi *et al.* reported a total βp intensity of $I_p = 1.6(7)\%$, an upper limit for $\beta\alpha$ intensity $I_\alpha \leq 0.023(20)\%$, and 5 ^{60}Ga$(\beta\gamma)$ transitions through 3 ^{60}Zn states. Orrigo *et al.* [33] confirmed these 5 $\beta\gamma$ transitions and proton-bound states and reported 24 new $\beta\gamma$ transitions that are correlated with ^{60}Ga implants. However, they did not place any of these new transitions in the decay scheme or provide any β-feeding intensities. Fig. 2 includes the weighted average of β-feeding intensities based on the 5 $\beta\gamma$ intensities reported by both studies [33, 38]. Unplaced $\beta\gamma$ transitions likely account for 26% of β-feeding intensities. A recent ^{60}Ga total absorption spectroscopy observed 15% of the β-feeding intensity above the ^{60}Zn proton separation energy [29], indicating the need for further measurements.

High-statistics ^{60}Ga β decay measurements with proton/α/γ-ray coincidences will allow for the construction of a more comprehensive decay scheme, including the proton/α-emitting states in ^{60}Zn and the ground and excited states of ^{59}Cu/^{56}Ni. This will provide crucial insights into the entrance and exit channels for the thermonuclear ^{59}Cu$(p,\gamma)^{60}$Zn and ^{59}Cu$(p,\alpha)^{56}$Ni reactions. Although β-decay spectroscopy has proved to be a powerful method for obtaining decay branching ratios, it typically does not provide lifetimes or widths of resonances. Therefore, employing PXCT-enhanced β-decay spectroscopy to obtain all essential information in a single experiment is highly desirable.

III. PARTICLE X-RAY COINCIDENCE TECHNIQUE

In the 1970s, the Particle X-ray Coincidence Technique (PXCT) was introduced and applied to measure the average lifetimes of proton-unbound states in ^{69}As populated by the electron capture (EC) of ^{69}Se [10]. The principle of the PXCT is illustrated in Fig. 3. In the process of an EC-delayed proton emission, a proton-rich precursor with an atomic number of Z decays by EC to the proton emitter $(Z-1)$. Due to the EC, a proton-unbound nuclear state and an atomic shell vacancy are created simultaneously. The vacancy is primarily created in the K shell. In the case of ^{60}Ga EC, the fractional

TABLE II. Gamow windows $\widetilde{E}_{\rm hi} - \widetilde{\Delta} \leq E \leq \widetilde{E}_{\rm hi}$ and Gamow peaks $\widetilde{E}_0$ for the ^{59}Cu$(p,\gamma)^{60}$Zn and ^{59}Cu$(p,\alpha)^{56}$Ni reactions at a temperature T [31].

	^{59}Cu$(p,\gamma)^{60}$Zn			^{59}Cu$(p,\alpha)^{56}$Ni		
T (GK)	$\widetilde{E}_{\rm hi} - \widetilde{\Delta}$ (MeV)	$\widetilde{E}_0$ (MeV)	$\widetilde{E}_{\rm hi}$ (MeV)	$\widetilde{E}_{\rm hi} - \widetilde{\Delta}$ (MeV)	$\widetilde{E}_0$ (MeV)	$\widetilde{E}_{\rm hi}$ (MeV)
0.5	0.51	0.71	0.92	0.55	0.74	0.98
1.0	0.67	0.91	1.26	0.73	1.01	1.48
1.5	0.75	1.01	1.57	0.87	1.27	2.11
2.0	0.82	1.14	1.83	1.01	1.74	2.80
2.5	0.85	1.40	2.05	1.24	2.19	3.52
3.0	0.89	1.49	2.26	1.51	2.66	4.16

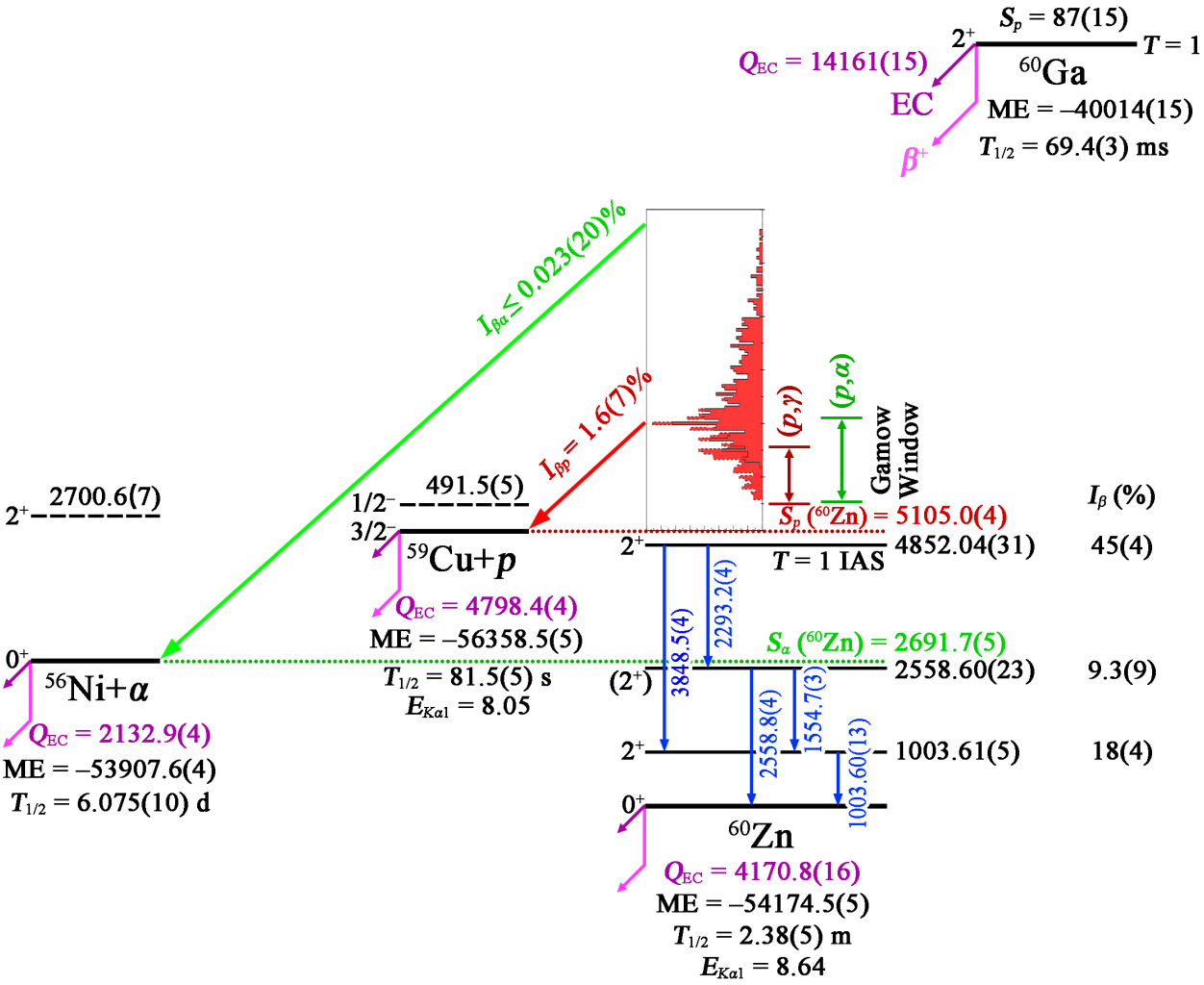

FIG. 2. Known decay scheme of ^{60}Ga. All energies are given in units of keV. The mass excesses, $Q_{\rm EC}$ values, and particle separation energies of ^{56}Ni, ^{59}Cu, and ^{60}Zn are from AME2020 [32], while for ^{60}Ga, these data are evaluated based on Refs. [33, 34]. The half-lives of ^{56}Ni, ^{59}Cu, and ^{60}Zn are from evaluations [35–37], respectively. The half-life of ^{60}Ga is evaluated based on Refs. [33, 38–42]. All spins and parities are adopted from evaluations [35–37], with the 4852-keV state in ^{60}Zn revised from (2^+) to 2^+ based on the unambiguous $T = 1$ isobaric analog state argument [33, 38]. The γ-ray energies, excitation energies, and β feedings of ^{60}Zn states are evaluated [43] based on all available measurements [33, 38, 44, 45]. The proton spectrum is adapted from Ref. [38]. The two dashed lines represent the first excited states of ^{56}Ni and ^{59}Cu, respectively, which have not been observed in ^{60}Ga decay. The double-headed arrows denote the Gamow windows for the ^{59}Cu$(p,\gamma)^{60}$Zn and ^{59}Cu$(p,\alpha)^{56}$Ni reactions at temperatures of 0.5−1.5 GK, respectively (Table II).

EC probability for the K shell is 89% [46]. An electron from an outer shell fills the K shell vacancy and may yield X-ray photons corresponding to the binding energy difference between the outer and the K shells. The K-shell fluorescence yield for Zn is 47%, with K_α X rays contributing 89% of all K X rays [47]. Meanwhile, the proton-unbound state with a comparable lifetime $\tau_{p-\mathrm{emit}}$ emits a proton to a state of the daughter $(Z-2)$. If the proton is emitted before the X-ray emission, then the X-ray energy will be characteristic of the daughter $(Z-2)$. If the proton is emitted after the X-ray emission, then the X-ray energy will be characteristic of the proton emitter $(Z-1)$. By measuring X rays in coincidence with protons, the relative intensities of the $(Z-1)$ and $(Z-2)$ X-ray peaks $I_{K_\alpha(Z-1)}/I_{K_\alpha(Z-2)}$, can be used to establish the relationship between the nuclear and atomic lifetimes:

$$\frac{\tau_{p-\mathrm{emit}}}{\tau_{K\mathrm{shell}(Z-1)}} = \frac{\Gamma_{K\mathrm{shell}(Z-1)}}{\Gamma_{p-\mathrm{emit}}} = \frac{I_{K_\alpha(Z-1)}}{I_{K_\alpha(Z-2)}}, \qquad (5)$$

where the level widths $\Gamma_{K\mathrm{shell}}$ and $\Gamma_{p-\mathrm{emit}}$ are the equivalent of $\hbar/\tau_{K\mathrm{shell}}$ and $\hbar/\tau_{p-\mathrm{emit}}$, respectively, as they both follow the exponential decay law. The lifetimes of proton-emitting states can be determined by measuring X-ray intensity ratios combined with known atomic K-shell vacancy lifetimes, ranging from 1.1×10^{-14} s for C ($Z=6$) down to 5×10^{-18} s for Fm ($Z=100$) [47–51]. This also defines the PXCT applicable lifetime range, where alternative approaches are limited [52]. The preceding discussion is also generalizable to EC-delayed α-particle emission, where the proton-decay daughter $(Z-2)$ is replaced by α-decay daughter $(Z-3)$. Another decay channel is EC-delayed γ-ray emission, which can occur either before or after the filling of atomic shell vacancies. However, the resulting X rays are always characteristic of $(Z-1)$ and are therefore insensitive for determining nuclear lifetimes.

So far, the PXCT has been applied in the decay studies of six nuclei, as summarized in Table III. By reproducing the average behavior and variance of the observed proton energy distribution and the X-ray count ratios as a function of coincident proton energies using the statistical model, the model correction parameters, such as the level density parameter (a), the correction factor for γ-ray partial widths (K_{T_ℓ}), and the correction factor for proton transmission coefficients (C_{Γ_γ}), can be constrained [54, 57, 59, 65]. These parameters can then be applied to determine the proton transmission coefficients (T_ℓ), proton partial widths (Γ_p), γ-ray partial widths (Γ_γ), and the level density (ρ):

$$\Gamma_p = \frac{\sum_\ell T_\ell(E_p)}{2\pi\rho_J(E_x)}, \qquad (6)$$

where $T_\ell(E_p)$ is the transmission coefficient for protons with energy E_p and angular momentum ℓ, and $\rho_J(E_x)$ is the level density with spin J at excitation energy E_x. The initial $T_\ell(E_p)$ is usually from the optical model calculations.

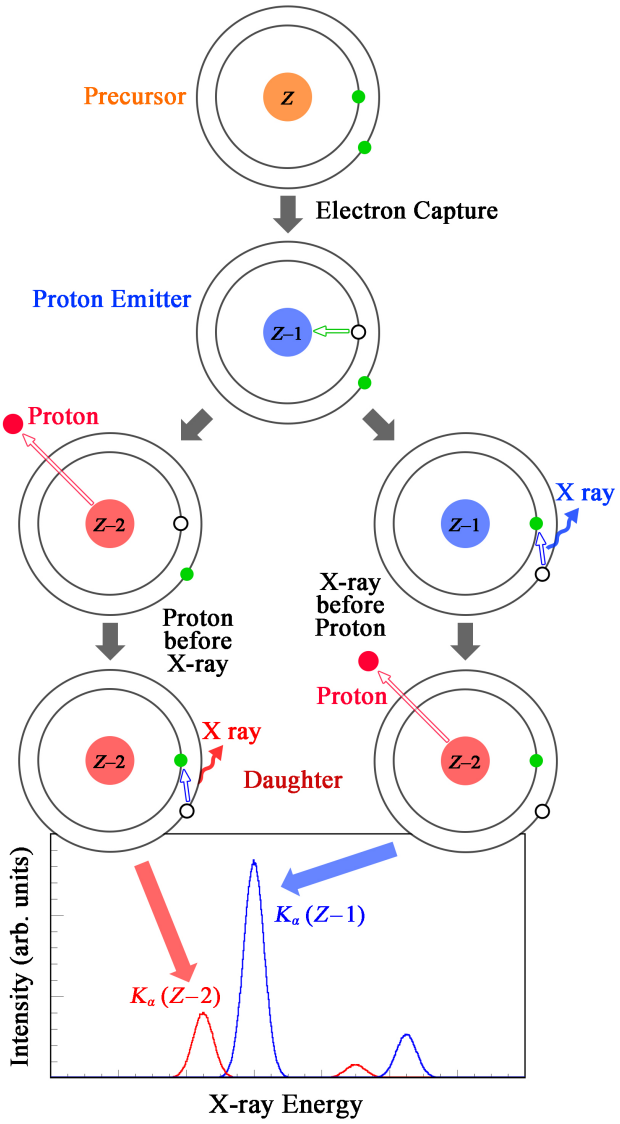

FIG. 3. Schematic illustrating electron capture to a proton-unbound excited state and the Particle-X-ray Coincidence Technique.

$$\Gamma_\gamma = \int_0^{E_x} E_\gamma^3 f_{E1}(E_\gamma) \sum_{I=J-1}^{J+1} \frac{\rho_I(E_x-E_\gamma)}{\rho_J(E_x)} \mathrm{d}E_\gamma, \qquad (7)$$

where $\rho_J(E_x)$ is the level density with spin J at excitation energy E_x, $\rho_I(E_x-E_\gamma)$ is the level density with spin I populated by the γ transition with energy E_γ. This expression is under the assumption that $E1$ transitions dominate the electromagnetic deexcitation. f_{E1} is the γ-ray strength function.

The level density is estimated with the back-shifted Fermi gas model [74]:

$$\rho_J(E_x) = \frac{2J+1}{24\sqrt{2}\sigma^3 a^{1/4}} \frac{\exp\left[2\sqrt{a(E_x-\Delta)} - \frac{J(J+1)}{2\sigma^2}\right]}{(E_x-\Delta+t)^{5/4}} \tag{8}$$

with

$$\sigma = 0.015 t A^{5/3} \quad t = \frac{1+\sqrt{1+4a(E_x-\Delta)}}{2a}, \tag{9}$$

where a is the level density parameter and Δ is the energy shift parameter [75].

In all six cases, only the average lifetimes of proton-unbound states populated by EC were obtained. Individual proton-emitting states could not be fully resolved due to high level densities. Moreover, the applicability of this technique has not been explored in an astrophysical context. We have designed and built a detection system to extend the PXCT to measure all essential ingredients for calculating reaction rates with the Hauser-Feshbach statistical model Eq. (4) [8]. This system may also be able to identify individual resonances, providing spin and parity, excitation/resonance energies, lifetimes, and decay branching ratios for narrow resonance reaction rate calculations using Eqs. (1) and (3).

IV. EXPERIMENTAL SETUP

A. Beam delivery

For the future experiment under consideration, the Facility for Rare Isotope Beams (FRIB) linear accelerator [76] will accelerate ^{70}Ge to 249 MeV/u with a beam power up to 400 kW. The reaction products from ^{70}Ge impinging on a rotating carbon transmission target will be separated in-flight by the Advanced Rare Isotope Separator [77]. A cocktail fast beam containing ^{60}Ga and some nearby isotones will be slowed down in metal degraders with momentum compression and thermalized in gas stoppers filled with helium [78, 79]. The thermalized ^{60}Ga ions will by drifted by a combination of radio-frequency and direct-current fields towards a nozzle and exit into a radio-frequency quadrupole ion-guide system. The ions will be guided and accelerated to 30 keV before being delivered to the stopped beam area [80]. The intensity of the ^{60}Ga stopped beam is estimated to be up to 9×10^3 pps.

As shown in Fig. 4, we have designed and built a PXCT detection system that will be used in the stopped beam area. Prior to the experiment, a stable beam around the $A = 60$ region will be tuned into the Faraday cup at the center of the vacuum chamber. After maximizing the beam current, the chamber will be vented and the Faraday cup will be replaced by an aluminized Mylar foil tilted at a 45° angle with respect to the beam direction. The ^{60}Ga beam will then be directed into the center of the foil. A 30-keV ^{60}Ga beam can be fully stopped by a Mylar foil as thin as 50 nm [81], in contrast to the 6.5 mm needed to stop the 130-MeV/u ^{60}Ga fast beam, which would block the emitted X rays and charged particles.

B. Detectors

The detection system is comprised of a planar germanium detector for X-ray detection, two large-volume coaxial germanium detectors for γ-ray detection, and a silicon telescope for charged-particle detection via energy-loss and residual energy (ΔE-E). The detection setup can provide real-time signals on characteristic charged particles and γ rays from decay, facilitating online radioactive beam optimization.

For X-ray detection, we selected a disc-shaped Low Energy Germanium detector (LEGe), Mirion GL0510 [82]. The LEGe detector consists of a Ge crystal with a diameter of 25.0 mm and a thickness of 10.5 mm. LEGe is housed in a flanged-style cryostat with a diameter of 38.1 mm and a 0.13-mm thick Be entrance window. The endcap is inserted into the vacuum chamber with its entrance window 11.0 mm from the center of the chamber. The Ge crystal is positioned 5.6 mm from the entrance window, subtending 10.1% of the 4π solid angle. LEGe is fabricated with a thin p^+ contact on the front and side, and a rear n^+ contact that covers less than the full area, resulting in lower capacitance than a similar-sized planar device. Since preamplifier noise is a function of detector capacitance, the low capacitance feature makes LEGe ideally suited for X-ray spectroscopy down to 3 keV.

For γ-ray detection, we selected two Extended Range Coaxial Germanium Detectors (XtRa), Mirion GX10020 [83]. The active volume of XtRa1 has a diameter of 84.8 mm and a thickness of 65.2 mm, while XtRa2 has a diameter of 79.8 mm and a thickness of 80.0 mm. The Ge crystals are positioned 6.8 and 6.3 mm, respectively, from the 0.6-mm-thick carbon composite windows. XtRa detectors feature a thin window contact on the front surface and a n^+ contact on the periphery, providing a good low-energy response.

All three Ge detectors are equipped with the Cryo-Pulse 5 Plus electrically refrigerated cryostat [84, 85]. The detector housing is connected to a compact cold-head assembly containing a 5-watt pulse tube cooler. The assembly is powered by a bench-top controller, which contains the necessary logic to ensure the safe and reliable operation of the cryostat. During normal operations, the cold tip is maintained at the preset −185 °C. If the cold tip temperature rises above −160 °C, the controller will trigger the high-voltage inhibit. If it further rises above −150 °C, the controller will shut down the cooler, forcing the Ge to undergo a full thermal cycle. Once the cold tip temperature reaches 0 °C, the cooler will restart. Additionally, a control panel application is included for

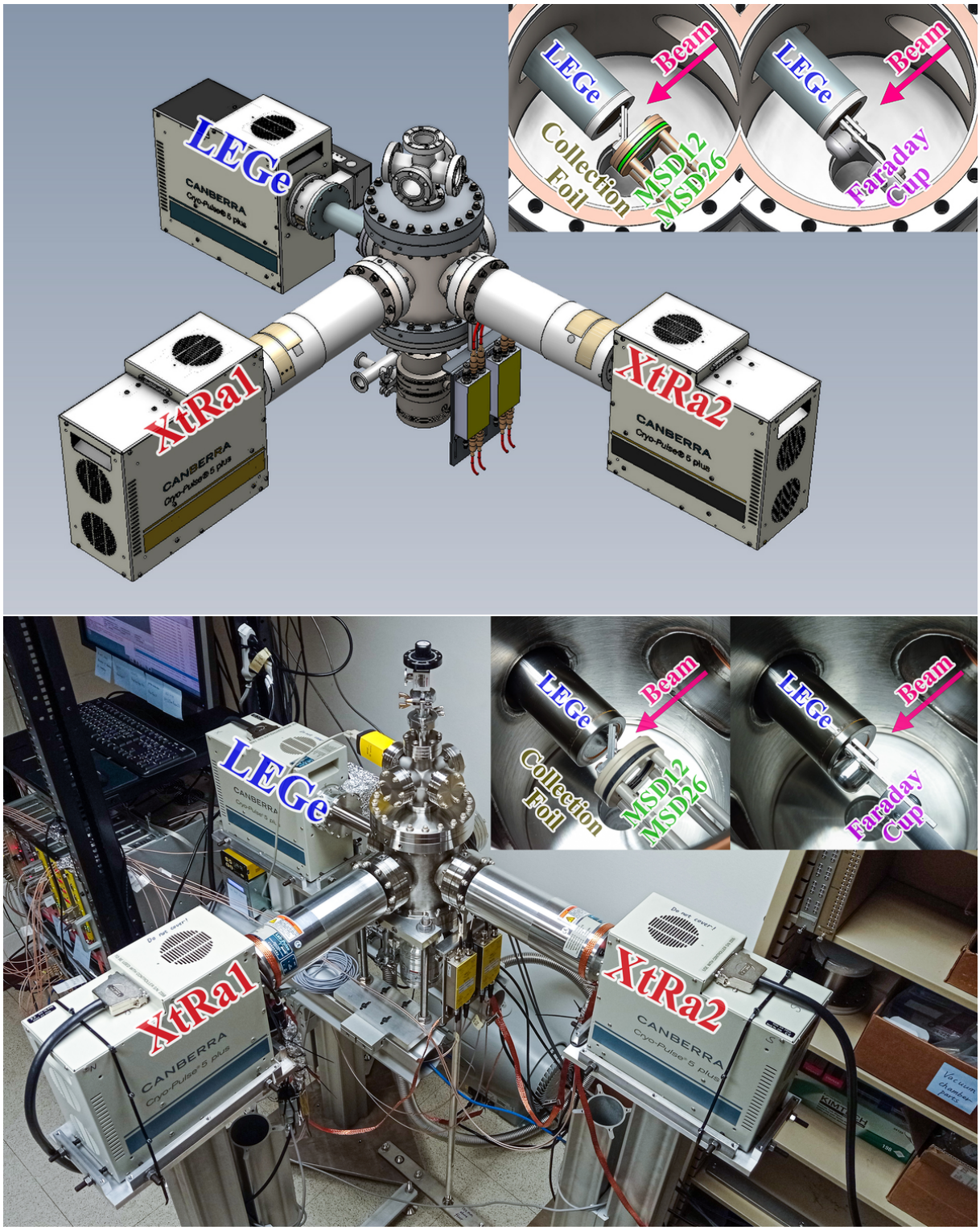

FIG. 4. Mechanical design drawing and photograph of the PXCT detection system. The insets highlight two configurations for the detectors inside the central chamber: a Faraday cup with a collimator for beam tuning or a collection foil and Si detectors for decay measurements.

TABLE III. Properties of all nuclei that have been measured with PXCT. Columns 1−7 present the EC/β^+ decay, the half-life ($T_{1/2}$) of the precursor, the β-decay energy ($Q_{\rm EC}$), the proton-separation energy of the EC/β^+-decay daughter (S_p), the total intensity of EC/β^+-delayed protons (I_p), the primary X-ray energies that need to be distinguished ($E_{K\alpha}$) for $(Z-2)$ and $(Z-1)$, the known lifetime of the K-shell vacancy, and the lifetime range of proton-emitting states of the EC/β^+-decay daughter obtained in each study, respectively. The last two rows list the properties of ^{60}Ga and ^{64}As for comparison.

EC/β^+-decay	$T_{1/2}$ (s)	$Q_{\rm EC}$ (keV) [32]	S_p (keV) [32]	I_p (%)	$E_{K\alpha}$ (keV) [105]	$\tau_{K\rm shell}$ (fs) [51]	$\tau_{p-\rm emit}$ (fs)
^{65}Ge→^{65}Ga	30.9(5) [53]	6179.3(23)	3942.4(6)	0.011(3) [54–56]	8.6, 9.2	0.374	∼1.7 [57]
^{69}Se→^{69}As	27.4(2) [58]	6680(30)	3420(30)	0.052(10) [59, 60]	9.9, 10.5	0.315	0.3−3.3 [10, 54, 59]
^{73}Kr→^{73}Br	27.3(10) [61]	7094(9)	3067(7)	0.47(22) [62, 63]	11.2, 11.9	0.264	0.3−2.7 [54, 64, 65]
^{77}Sr→^{77}Rb	9.0(2) [66]	7027(8)	3106(4)	0.08(3) [54, 55]	12.6, 13.4	0.222	∼1.5 [54]
^{113}Xe→^{113}I	2.74(8) [67]	8916(11)	841(12)	7(4) [68]	27.5, 28.6	0.062	0.3−2.9 [68]
^{117}Ba→^{117}Cs	1.75(7) [69]	9040(260)	740(60)	16(3) [70]	29.8, 31.0	0.054	>4.7 [70]
^{60}Ga→^{60}Zn	0.0694(3)[a]	14161(15)[a]	5105.0(4)	1.6(7) [38]	8.0, 8.6	0.406	
^{64}As→^{64}Ge	0.0690(14) [71]	14606(110)[b]	5057(4)	unreported [73]	9.2, 9.9	0.343	

[a] See Fig. 2 for evaluation details.
[b] Deduced based on ^{64}As mass [72] and ^{64}Ge mass [32].

remote control, monitoring, and logging of the cryostat status.

For the ΔE-E charged-particle telescope, we selected two single-sided, single-area circular Si detectors manufactured by Micron Semiconductor Ltd. The active area of MSD12 is 12 μm thick and 12 mm in diameter [86], and MSD26 is 1000 μm thick and 26 mm in diameter [87]. The junction side of both MSDs features a 50-nm thick boron-doped silicon dead layer and a 30-μm wide peripheral metal band for wire bonding, leaving the majority of the active area without metal coverage. The Ohmic side of MSD12 has a thicker dead layer of 300 nm with no metal coverage. The Ohmic side of MSD26 has little impact on charged-particle signals, and thus, we opt for the standard 500-nm thick dead layer and 300-nm thick aluminum coverage. Both silicon chips are assembled onto an FR4 printed circuit board. MSD26 is positioned 15.7 mm from the center of the chamber and covers 11.5% of the 4π solid angle. MSD12 is 11.2 mm from the center and defines the solid angle coverage of the ΔE-E telescope at 5.9% of 4π.

C. Electronics

All three Ge detectors are equipped with the Intelligent Preamplifiers (iPA) [88], which incorporate a low-noise field-effect transistor (FET) input circuit optimized for the ultra-high source impedance of Ge detectors. The first stage of the iPA functions as an integrator and an electrometer, providing an output voltage proportional to the accumulated charge and measuring the leakage current. The second stage of the iPA acts as an output buffer and provides four selectable gain settings. The iPA provides remote monitoring and logging of the detector leakage currents, temperatures, and preamplifier operating voltages. Each iPA is equipped with two 100-Ω Pt resistance temperature detectors thermally connected to the crystal holder (PRTD1) and the cold tip (PRTD2), respectively [89]. In our lab testing environment, the observed PRTD1 temperatures are −182.7 °C (LEGe), −158.1 °C (XtRa1), and −168.2 °C (XtRa2), respectively, which represent the temperatures of the Ge crystals when they are in thermal equilibrium. The nominal PRTD1 temperatures are −182.6 °C (LEGe), −163.6 °C (XtRa1), and −170.9 °C (XtRa2), respectively. If either PRTD exceeds its nominal value by 10 °C, it can trigger the high-voltage inhibit via the iPA. This mechanism operates independently of the inhibit function via the controller, providing enhanced protection for the detector.

Two ORTEC 660 Dual Bias Supply modules [90] are used to provide bias voltages to the three Ge detectors. We apply a negative bias to the p^+ contacts of LEGe and a positive bias to the n^+ contacts of XtRa. LEGe becomes fully depleted at −600 V and is recommended to be operated at −1100 V. XtRa1 and XtRa2 become fully depleted at a bias voltage of +4000 V and +2200 V, respectively, and both operate at +4500 V. The bias shutdown mode of ORTEC 660 is configured to be compatible with the iPA high-voltage inhibit mode. The typical leakage currents of the two XtRa detectors are below 20 pA and below 100 pA for LEGe. A Mesytec MHV 4-channel bias supply module with remote control features provides the bias voltages to the two MSD Si detectors. We apply a negative bias to the p^+ contacts of both MSD detectors through MPR-1 charge-sensitive preamplifiers [91] and the n^+ contacts are grounded. MSD12 has a depletion voltage of −1.5 V and is operated at −3.0 V, and MSD26 has a −90 V depletion voltage and is operated at −130 V. MHV offers a ramp speed as low as 5 V/s to protect the circuits of preamplifiers [92]. MSD26 has a leakage current of approximately 60 nA, whereas MSD12 maintains a leakage current below 1 nA.

All the preamplifiers are powered by two Mesytec MNV-4 NIM power distribution and control modules [93].

D. Data acquisition

All the preamplifier signals are transmitted via double-shielded RG316 coaxial cables of equal length and then digitized by a 16-bit, 250 MHz Pixie-16 module manufactured by XIA LLC [94]. The input impedance of each channel in Pixie-16 is configured to be 1 kΩ. The Digital Data Acquisition System (DDAS) is used [95, 96] for recording and processing data. Trapezoidal filtering algorithms are implemented in both the slow filter for pulse amplitude measurement and the fast filter for leading-edge triggering. Each event is timestamped using a Constant Fraction Discriminator (CFD) algorithm based on the trigger filter response. The system operates in an internally triggered mode: recording data on a channel-by-channel basis whenever the trigger filter crosses the user-defined threshold. The data from all channels is ordered in time and subsequently assembled into events based on a user-defined event window length. The event timestamp is counted with 125 MHz clock ticks, i.e., 8 ns intervals.

The tail pulses from MPR-1 exhibit rise times of 400 ns (MSD12) and 70 ns (MSD26), with a 120 μs decay constant. The tail pulses from iPA exhibit rise times of 150 ns (LEGe) and 250 ns (XtRa), with a 50 μs decay constant. The DDAS filter parameters are optimized based on these observations [96–99]. The pulse amplitude is extracted from the energy filter amplitude at approximately rise time plus gap time after triggering. If a second trigger arrives within the rise time plus gap time window, both events will be flagged as pile-up. The energy filter parameters are the dominant factor in determining the count rate capacity of the DDAS system.

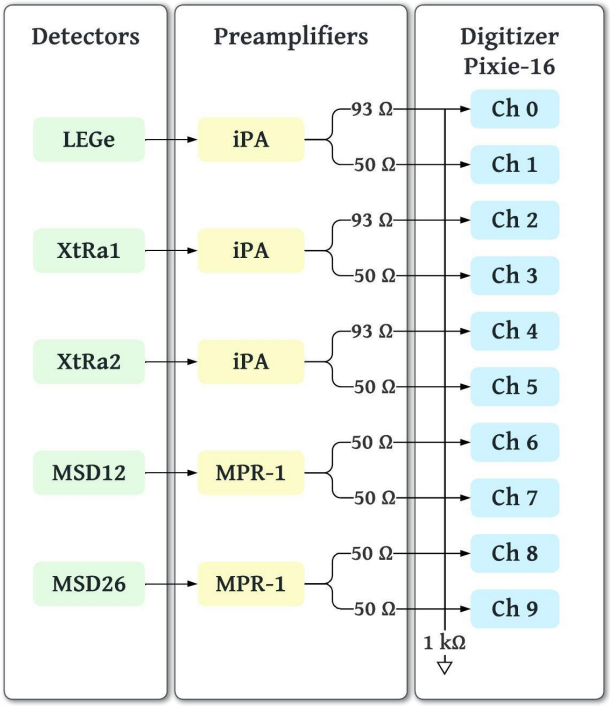

FIG. 5. Schematic diagram of the electronics setup. The two arrows following each preamplifier indicate dual outputs with their respective impedance.

V. PERFORMANCE TESTS

We have performed comprehensive tests on the PXCT system using the electronics configuration illustrated in Fig. 5.

A DB-2 Random Pulser [100] was used to investigate the data acquisition dead time. The time intervals between successive pulses follow a Poisson distribution function. The count rate performance is shown in Fig. 6. The observed event losses are in line with the pile-up rates defined by the energy filter settings [95]. Considering the achievable stopped beam rates at FRIB, decay intensities, and detection efficiencies, no detector will need to process more than 1000 events per second in the ^{60}Ga decay experiments, and therefore, the maximum dead time for any detector will be less than 3%.

Table IV lists the characteristics of all radioactive sources used in the PXCT detector tests. A typical event-build window of ±1 μs was used, and the count

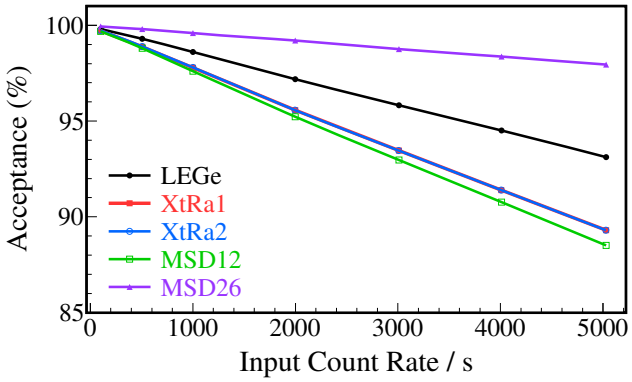

FIG. 6. DDAS count rate performance.

TABLE IV. Radioactive sources used in the PXCT detector tests. Columns two through seven present the source nuclides, main decay modes, actual activities (A), relative uncertainties of the activities (σA), active diameters (D), and half-lives ($T_{1/2}$), respectively.

No.	Nuclide	Decay	A (Bq)	σA (%)	D (mm)	$T_{1/2}$ (y)
1	^{55}Fe	EC	1.11×10^4	–[a]	9.5	2.74
2	^{60}Co	β^-	3.73×10^4	3	1	5.27
3	^{137}Cs	β^-	3.00×10^3	3	3	30.1
4	^{148}Gd	α	2.86×10^4	–[a]	5	71.1
5	^{152}Eu	EC/β^-	3.10×10^4	1.4	3	13.5
6	^{241}Am	α	3.44×10^3	2.7	3	432.6

[a] Unknown source activity uncertainties; not used for efficiency calibration.

rate of each detector remained below 1500 events per second throughout all conducted tests, except for the LEGe efficiency test with the ^{152}Eu source.

A. X-ray measurements

We evaluated the performance of LEGe using the ^{55}Fe, ^{152}Eu, and ^{241}Am sources, as shown in Fig. 7. ^{55}Fe EC decays to ^{55}Mn ground state, and the subsequent filling of atomic shell vacancies results in X rays characteristic of Mn. Similarly, Sm X rays mainly result from ^{152}Eu EC. ^{152}Eu decay populates ^{152}Sm/^{152}Gd excited states, which can deexcite via internal conversion (IC), followed by filling of atomic shell vacancies and the emission of X rays characteristic of Sm/Gd. This explains why the observed Gd X rays are much weaker compared to Sm X rays that have two production mechanisms: EC and IC. For ^{241}Am, α decay populates ^{237}Np excited states, where IC serves as the primary mechanism leading to Np X rays. A trace amount of X rays may also be produced through inner shell ionization and excitation caused by perturbations in the electron cloud during nuclear decays [101, 102]. The 0.13-mm thick Be entrance window is sufficient to block electrons below 125 keV [103], rendering the LEGe detector insensitive to Auger electrons.

The overall energy resolution achieved by LEGe is characterized by fitting X-ray or γ-ray lines with an exponentially modified Gaussian (EMG) function [104] to account for incomplete charge collection at 5.90 keV (Mn $K_{\alpha1}$), 6.49 keV (Mn $K_{\beta1}$), 11.89 keV (Np L_ℓ), 13.76 keV (Np $L_{\alpha2}$), 13.95 keV (Np $L_{\alpha1}$), 26.34 keV (^{237}Np γ), 33.20 keV (^{237}Np γ), 39.52 keV (Sm $K_{\alpha2}$), 40.12 keV (Sm $K_{\alpha1}$), 45.29 keV (Sm $K_{\beta3}$), 45.41 keV (Sm $K_{\beta1}$), and 59.54 keV (^{237}Np γ). We then interpolated the full width at half maximum (FWHM) values at the energies of interest, 8.05 keV (Cu $K_{\alpha1}$) and 8.64 keV (Zn $K_{\alpha1}$), to be 0.238(8) and 0.241(7) keV, respectively, demonstrating sufficient resolution to distinguish between the key X rays of Zn and Cu.

For photons below 100 keV interacting with Ge, the photoelectric effect is predominant, i.e., the photon is absorbed, and a photoelectron is ejected by the Ge atom. When the resulting atomic shell vacancy is filled, X rays characteristic of Ge may be created. A full-energy peak is still observed if these X rays are reabsorbed near the original interaction site. However, if the photoelectric interaction occurs near the surface of Ge, the X rays are more likely to escape, which results in peaks usually at 9.89 keV and 10.98 keV below the photopeaks, known as the Ge escape peaks (Fig. 7). These energy differences correspond to the characteristic $K_{\alpha1}$ and $K_{\beta1}$ X-ray energies for Ge, respectively [105].

We evaluated the detection efficiency of LEGe using the X rays from the ^{152}Eu source placed at the center of the chamber tilted at a 45° angle with respect to LEGe. ^{152}Eu emits Sm L X rays at 5.0 keV (L_ℓ), 5.6 keV (L_η, L_α), 6.2 keV (L_β), and 7.2 keV (L_γ). The Gd L X rays are approximately half a keV higher but with two orders of magnitude lower intensities. We adopted the total L X-ray emission probability from Ref. [107] and deduced the absolute intensities for each of the 4 groups of X rays based on the relative emission probabilities reported by Ref. [108]. The corresponding efficiencies are indicated by the 4 low-energy data points in Fig. 8. We also measured the X rays from the ^{241}Am source placed at the center of the chamber. ^{241}Am emits Np L X rays at 11.9 keV (L_ℓ), 13.9 keV (L_α), 15.9 keV (L_η), and 17.0 keV (L_β) [109]. The corresponding efficiencies are indicated by the 4 high-energy data points in Fig. 8.

We simulated the X-ray detection efficiencies using GEANT4 [110, 111]. The simulation incorporates the geometric configuration of the setup and the LEGe detector response, which was characterized by fitting the measured X-ray lineshapes in Fig. 7 with the EMG function. Monoenergetic X rays are emitted isotropically from the source position and interact with the surrounding materials. The simulation outputs an energy spectrum, from which we obtain the detection efficiency by dividing the counts in the X-ray peak by the number of emitted X rays. This process was repeated at different energies to generate the efficiency curves shown in Fig. 8.

For photon energies just above the K-shell binding energy of Ge, 11.1030(20) keV [105], the incident photon is strongly absorbed without deep penetration beyond the detector surface. The subsequent characteristic K X rays of 9.7−11.1 keV tend to escape. However, for photons just below the Ge K-shell binding energy, K-shell absorption is no longer possible, and L-shell interactions dominate. In this case, incident photons tend to penetrate somewhat deeper, and the chance of escape of the fluorescent Ge L X rays of 1.0−1.4 keV is significantly lower. This phenomenon abruptly changes the full-energy detection efficiency of X rays near the K-shell absorption edge [112]. The ^{241}Am source used

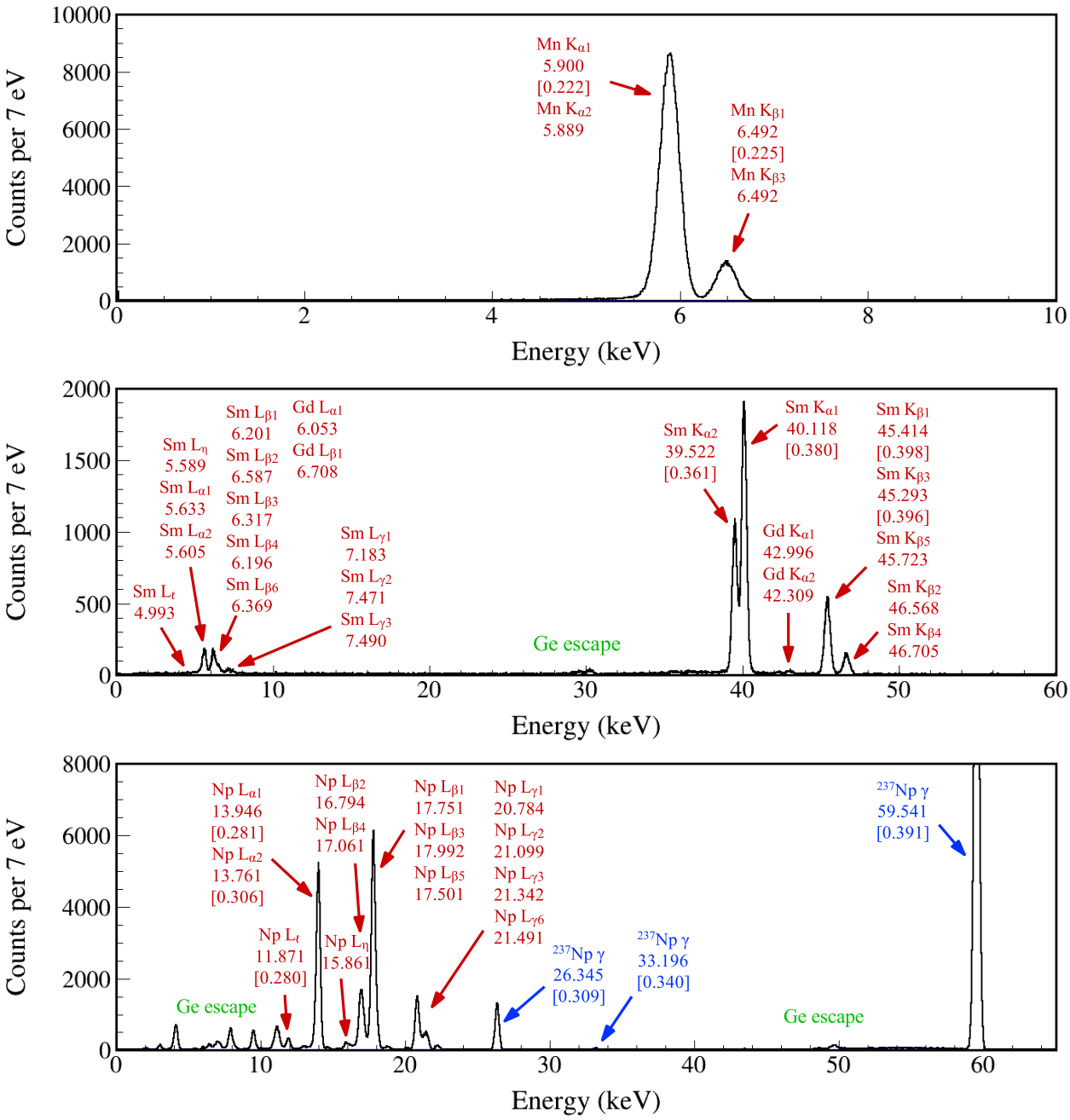

FIG. 7. X-ray and/or γ-ray spectra measured by the LEGe detector using the ^{55}Fe (top), ^{152}Eu (middle), and ^{241}Am (bottom) sources. X-ray energy values are adopted from Ref. [105] rounded to the nearest 0.001 keV. γ-ray energy values are adopted from Ref. [106] rounded to the nearest 0.001 keV. FWHM values used to characterize the energy resolution of LEGe are indicated within brackets.

for this test is an open source, while the ^{152}Eu source is encapsulated between two 60-μm thick Mylar tapes. The Mylar layer attenuates low-energy X-rays, but its impact diminishes for X rays above 10 keV. Additionally, the LEGe count rate was ~3000 pps during the ^{152}Eu test but only ~200 pps during the ^{241}Am test, resulting in different DAQ dead time (Fig. 6). Therefore, the ^{152}Eu efficiency curve represents a lower limit, while the ^{241}Am efficiency curve represents an ideal setting. The ^{60}Ga experimental condition is expected to fall between these two scenarios, and we estimate the X-ray efficiencies at 8.0 and 8.6 keV to be 6.5−7.4% and 7.0−7.8%, respectively.

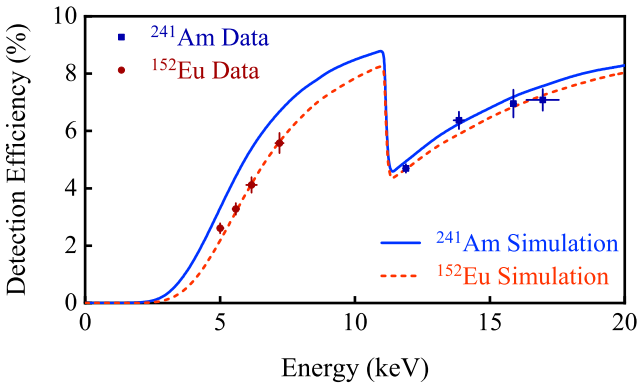

FIG. 8. Absolute X-ray photopeak detection efficiency of the LEGe detector obtained using the Sm L_ℓ, $L_\eta + L_\alpha$, L_β, and L_γ X rays from the ^{152}Eu source and Np L_ℓ, L_α, L_η, and L_β X rays from the ^{241}Am source, each placed at the center of the chamber. The red dashed and blue solid curves represent the GEANT4 simulated efficiencies according to the ^{152}Eu and ^{241}Am source configurations, respectively. The error bars along the x-axis also reflect the energy span for the multiple X rays within each group.

B. γ-ray measurements

Figure 9 shows the γ-ray spectra measured by XtRa1 and XtRa2 using the ^{152}Eu source. We first placed the source at the midpoint between the two XtRa detectors that were facing each other, with a distance of 28 cm between them. Both XtRa detectors exhibit good low-energy response to the ^{152}Sm X rays at 40 keV. We then placed the source at the center of the vacuum chamber to determine the absolute γ-ray detection efficiencies. The two XtRa detectors were placed as close as possible to the two flanges (Fig. 4), with their entrance windows about 12 mm from the flange surface. XtRa1 Ge crystal has a slightly larger diameter than XtRa2. Both Ge crystals are 158.5 mm from the target center, covering 1.70% and 1.51% of the 4π solid angle, respectively. Both XtRa detectors record an average of 300 room background γ rays per second in our lab test environment. The manufacturer specifies FWHM values for XtRa1 and XtRa2 as 0.998 and 1.065 keV at 122 keV (^{57}Co), and 1.879 and 1.926 keV at 1332 keV (^{60}Co), respectively. The insets of Fig. 9 demonstrate that the observed energy resolution using the ^{152}Eu source aligns with these specifications. The absence of X-ray peaks in the second test (lower panel of Fig. 9) is due to the 3.175-mm thick stainless steel flanges of the chamber effectively blocking the X rays.

We also measured the γ-ray detection efficiencies using the ^{60}Co and ^{137}Cs sources placed at the center of the chamber. MSD12 was not in place during these tests due to its fragility. MSD26 and the Si detector holders attenuated the γ rays from the source to XtRa2 but had little effect on XtRa1. Based on an exponential function that contains a polynomial of degree i with the natural logarithm of the energy E: $\varepsilon(E) = \exp\left[\sum_{i=0}^{6} p_i \ln(E)^i\right]$ [114] fit on all the data points, we obtain the photopeak efficiencies of 0.334(3)% and 0.286(3)% at 1 MeV, respectively, for XtRa1 and XtRa2. The error bars on the data points reflect the uncertainty of the γ-ray yields and the source activities, with an additional 2.5% uncertainty to account for the true coincidence summing effect [115, 116], which was estimated based on the observed 1173-1332-keV γ cascade from ^{60}Co.

We have used GEANT4 simulation [110, 111] to extend the γ-ray detection efficiency curve to high energies (Fig. 10). The simulation takes into account the geometry of the setup and the detector response characterized by fitting the measured γ-ray lineshapes with the EMG function. Monoenergetic γ rays were emitted isotropically according to the source distribution and interacted with the surrounding materials. The photopeak efficiency was extracted from the output spectrum. We then fit the ratio of the simulated efficiency to the measured efficiency between 0.5−1.5 MeV and obtained energy-independent ratios of 0.875(10) and 0.837(10) for XtRa1 and XtRa2, respectively, which serve as the normalization factors to match the simulation with the experimental data. One of the factors that reduces the measured efficiency is the data acquisition event loss, which is estimated to be 3.3%, 0.7%, and 2.1% based on the count rates during the ^{60}Co, ^{137}Cs, and ^{152}Eu tests, respectively (Fig. 6).

The mechanical design allows for the versatile combination of individual detectors for various experimental purposes. The two XtRa detectors have been coupled with a silicon cube [117] and with a Time Projection Chamber [118]. We also have the option to engineer the integration of LEGe and the central chamber with larger germanium detector arrays, such as the DEcay Germanium Array initiator (DEGAi) and ultimately DEGA [119], to achieve a higher γ-ray detection efficiency.

C. Charged-particle measurements

Figure 11 shows the α spectrum measured by MSD26 alone using the ^{241}Am source, with a 2-mm diameter aperture installed in front. An EMG fit of the main peak at 5485.56 keV yields a FWHM value of 17.0 keV, corresponding to an energy resolution of 0.31%. MSD12 alone is too thin to stop α particles above 3 MeV, and we demonstrate the ΔE-E α spectra measured by the telescope formed by MSD12 and MSD26 in Fig. 12. An EMG fit of the energy-sum peak yields a FWHM value of 52.1 keV, corresponding to an energy resolution of 0.95%.

We installed MSD26 and calibrated it using the ^{148}Gd (E_α = 3182.68 keV [120]) and ^{241}Am sources, and then measured the residual energy of ^{241}Am α particles in

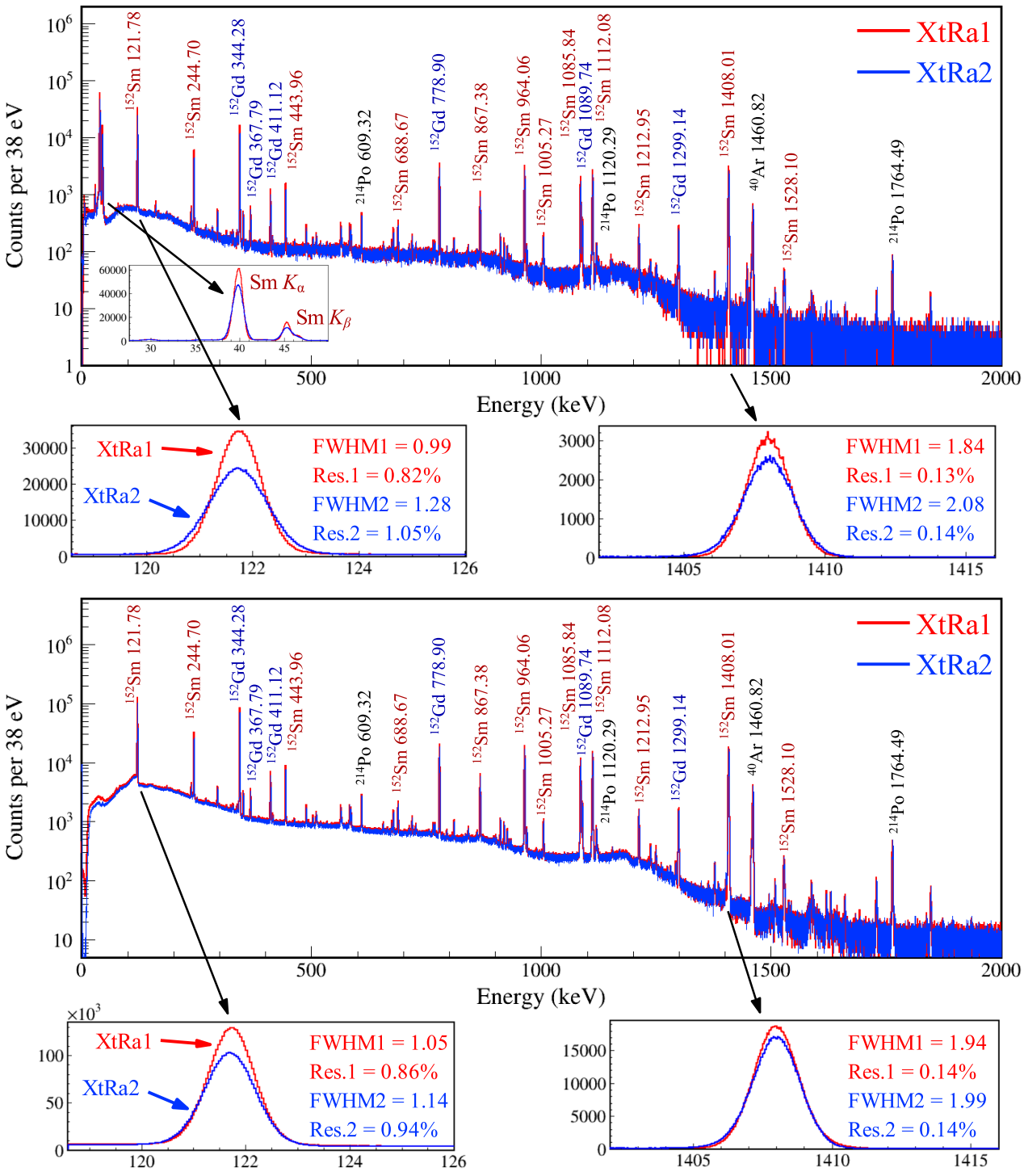

FIG. 9. γ-ray spectra measured by XtRa1 (red) and XtRa2 (blue) using the ^{152}Eu source. Upper panel: the ^{152}Eu source is placed in the middle of the two XtRa facing each other. Lower panel: the ^{152}Eu source is placed at the center of the vacuum chamber, with the two XtRa detectors positioned according to the Fig. 4 configuration. All the γ-ray energy values are adopted from Ref. [113] rounded to the nearest 0.01 keV. The insets demonstrate the detector responses at 122 and 1408 keV.

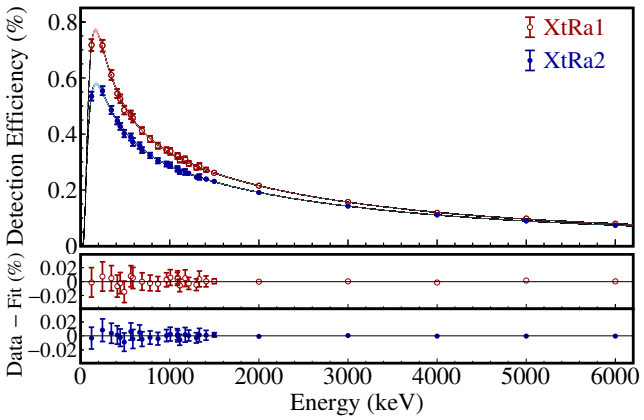

FIG. 10. Absolute γ-ray photopeak detection efficiency of the two XtRa detectors obtained using the ^{152}Eu, ^{137}Cs, and ^{60}Co sources placed at the center of the chamber. The ^{137}Cs data point at 662 keV is only applicable to XtRa2 due to the source placement. The 6 data points above 1408 keV are GEANT4 simulated efficiencies scaled by a factor to match the low-energy source data. The efficiency curves are generated by fitting all measured and simulated data points.

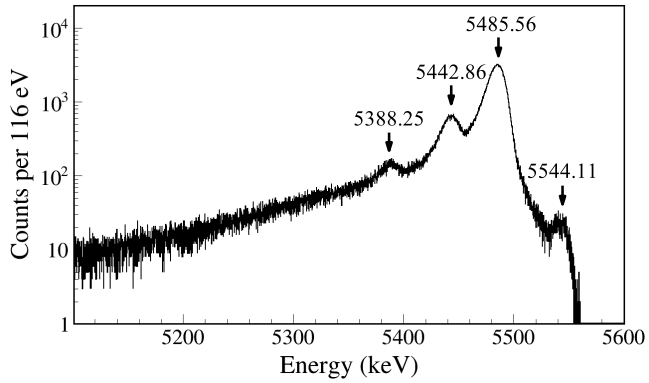

FIG. 11. α spectrum measured by MSD26 using the ^{241}Am source. The α energy values are adopted from Ref. [109] rounded to the nearest 0.01 keV. The FWHM value at 5485.56 keV is 17.0 keV, corresponding to an energy resolution of 0.31%.

MSD26 with MSD12 installed in front of it. This allowed us to accurately determine the effective thickness of MSD12 to be 11.65(8) μm after subtracting the 0.35-μm dead layer thickness [81]. The total thickness of MSD12 is in agreement with the nominal value of 12 μm specified in the Micron datasheet [86].

D. Electron measurements

Figure 13 shows the electron spectra measured by MSD26 using the ^{137}Cs source placed at the center of the chamber facing MSD26. The source is deposited on

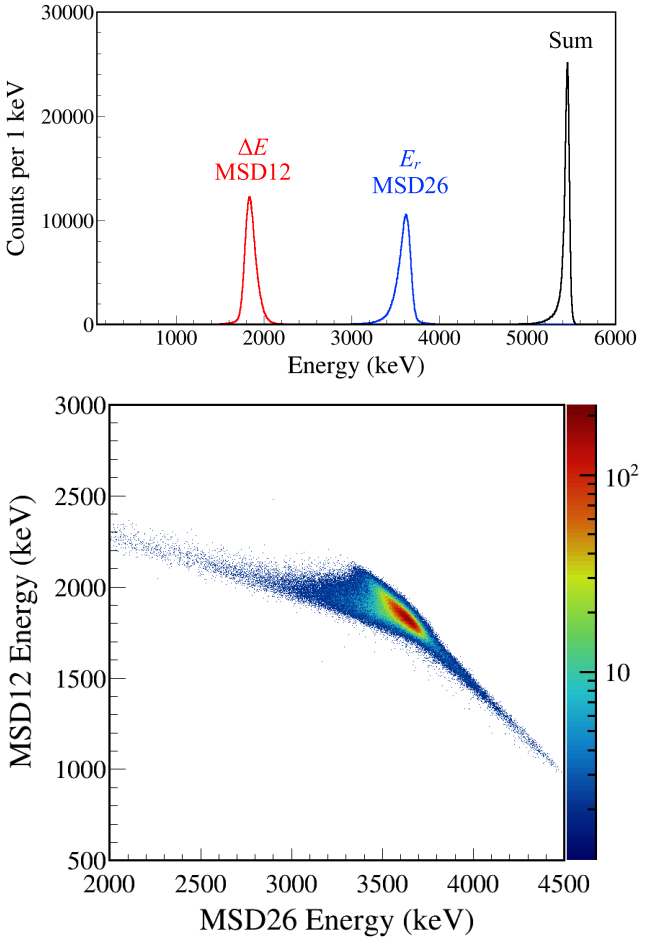

FIG. 12. Upper: ^{241}Am α-energy spectra measured by MSD12 (energy-loss) and MSD26 (residual energy). The FWHM value of the sum peak is 52.1 keV, corresponding to an energy resolution of 0.95%. Lower: ΔE-E 2D plot.

a 64.4-μm thick aluminized Mylar disk and covered with a 6.3-μm thick Kapton window. The spectrum exhibits a continuum of electrons from ^{137}Cs β^- decay, along with distinct electron peaks from IC. The main β^- decay branch has an endpoint energy of 514 keV and the IC peaks are characterized by the energy differences between the 662-keV ^{137}Ba isomeric transition and the Ba atomic shell binding energies. Using the total intensity of IC electrons of 9.56(14)% per ^{137}Cs decay [121] and the source activity (Table IV), we estimate the detection efficiency of MSD26 alone to be 9.0(3)%.

E. Coincidence measurements

Figure 14 shows the α-γ coincidence spectrum between the MSD telescope and LEGe with the ^{241}Am source placed at the center of the chamber. The source faces the MSD, and its 127-μm-thick Pt substrate attenuates most of the low-energy photons emitted towards LEGe,

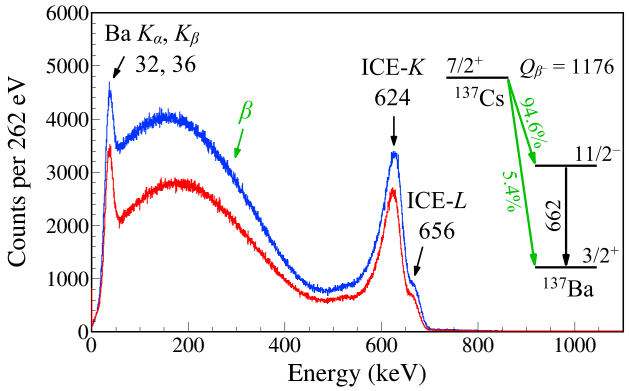

FIG. 13. Electron spectra measured by MSD26 using the ^{137}Cs source. The spectrum with lower statistics (red) was obtained with MSD12 installed between the source and MSD26. The spectrum with higher statistics (blue) was acquired over an equal time period with MSD12 removed. Electrons from ^{137}Cs β^- decay form the continuum. ICE-K and ICE-L denote the internal conversion electrons ejected from Ba K and L atomic shells, respectively. The low-energy peak is mainly from Ba K_α X rays at 32 keV and K_β X rays at 36 keV. All energy values are adopted from Ref. [121] rounded to the nearest keV. A simplified ^{137}Cs decay scheme shows the main decay branches.

leaving mainly the 59.5-keV ^{237}Np γ ray and its escape peaks observable.

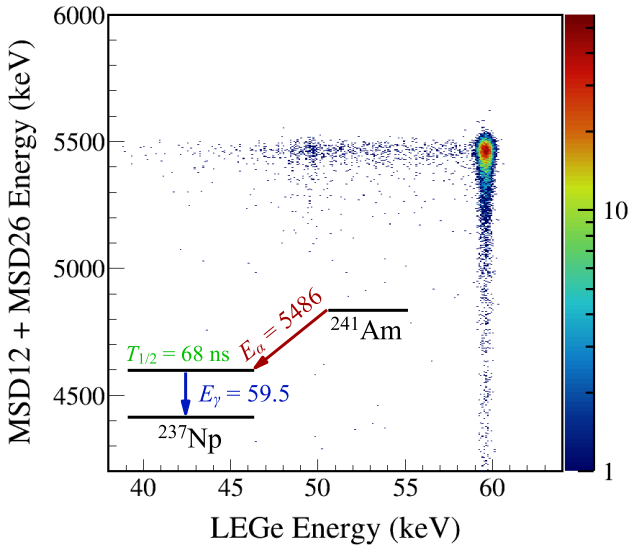

FIG. 14. Coincidence spectrum between the MSD detector telescope and LEGe obtained using the ^{241}Am source placed at the center of the chamber. A simplified ^{241}Am decay scheme shows the dominant α-γ sequence.

We placed the ^{152}Eu source at the center of the chamber. Figure 15 shows the XtRa1 γ spectra gated by the Sm K X rays measured by LEGe and gated by the electrons measured by MSD26, respectively. By applying the characteristic X-ray coincidence condition, both the room background γ rays and the ^{152}Gd γ rays are substantially suppressed. Conversely, the electron coincidence condition suppresses the room background and the ^{152}Sm γ rays. Having the ability to detect electrons and positrons would help clean up the in-beam spectrum, thereby facilitating the identification of γ ray origins.

F. Timing performance

The timing performance of the electronics was first tested using a Canberra Model 1407P Pulse Pair Generator [122]. The dual pulses were separately fed into two Pixie-16 channels. The FWHM resolution of the time-difference distribution is estimated to be 0.46 ns. Then, the primary pulse was split and fed to each test input of preamplifiers, and the resulting FWHM timing resolutions are 37.4 ns (MSD12), 4.4 ns (MSD26), 1.2 ns (XtRa1), and 1.8 ns (XtRa2).

The timing performance of the detectors was studied using each of the ^{60}Co, ^{152}Eu, ^{241}Am sources placed at the center of the chamber. ^{60}Co provides γ-γ coincidences to test the two XtRa detectors, ^{152}Eu provides X-γ coincidences to test LEGe and XtRa, and ^{241}Am provides α-γ coincidences to test MSD and LEGe. Figure 16 shows the time difference distributions between each coincidence. Based on these measurements, an event-build window of a few hundred ns can be defined to capture all prompt coincidences and some chance continuum for background subtraction in offline analysis. The asymmetric tail in both α-γ time difference distributions is attributed to the relatively long-lived 59.5-keV excited state of ^{237}Np.

Figure 17 shows the α-γ time difference distribution constructed by the start timestamps from 5486-keV α measured by the two MSDs and the stop timestamps from the 59.5-keV γ ray deexciting the 59.5-keV state in ^{237}Np measured by LEGe. By fitting the time spectra with a function

$$f(t; N, T_{1/2}, B) = \frac{N \ln(2)}{T_{1/2}} \exp\left[-\frac{t \ln(2)}{T_{1/2}}\right] + B \qquad (10)$$

composed of the total number of decays (N), the exponential decay half-life ($T_{1/2}$), and a constant background (B), we obtained the half-life of the 59.5-keV excited state in ^{237}Np to be 68.1(6) ns (MSD12) and 67.9(5) ns (MSD26), respectively. Two factors may limit the time resolution that can be achieved with semiconductor detectors. Firstly, the charge collection process is inherently slow, typically taking several hundred nanoseconds. This timescale is much longer than the output from scintillators, making it hard to achieve the same level of timing performance. Secondly, the pulse rise shape from semiconductor detectors can

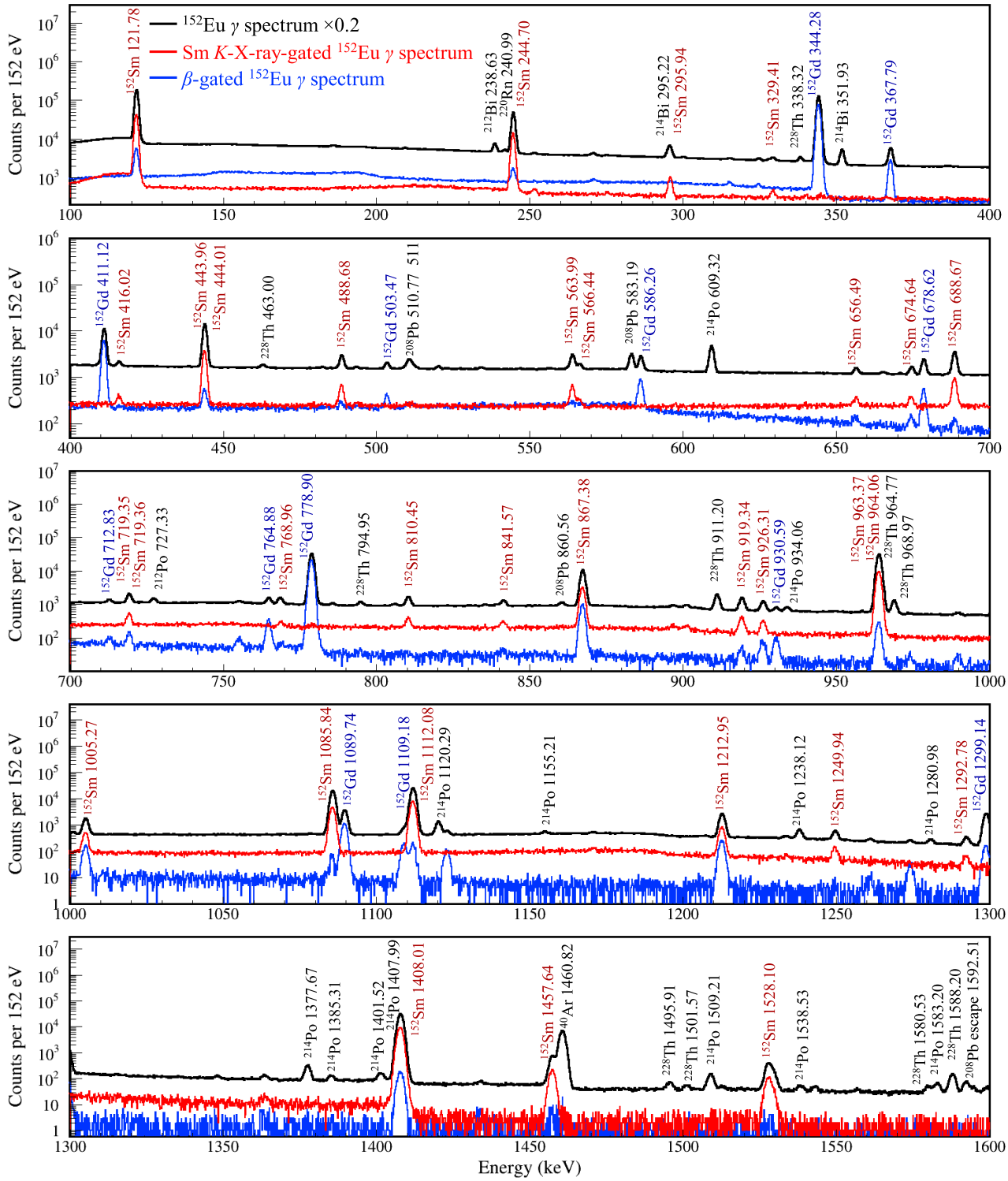

FIG. 15. Black represents the raw γ-ray spectrum measured by XtRa1 using the ^{152}Eu source placed at the center of the chamber. Red represents the XtRa1 γ-ray spectrum gated by the Sm K_α and K_β X rays measured by LEGe. Blue represents the XtRa1 γ-ray spectrum gated by the electrons measured by MSD26. The raw spectrum is scaled down by a factor of 5 for better comparison.

vary significantly from event to event, resulting in a larger uncertainty in generating timestamps. Nevertheless, the results obtained from both Si detectors are consistent with recent precision measurements of 67.86(9) ns [123] and 67.60(25) ns [124], thereby providing some level of validation for the PXCT electronics configuration.

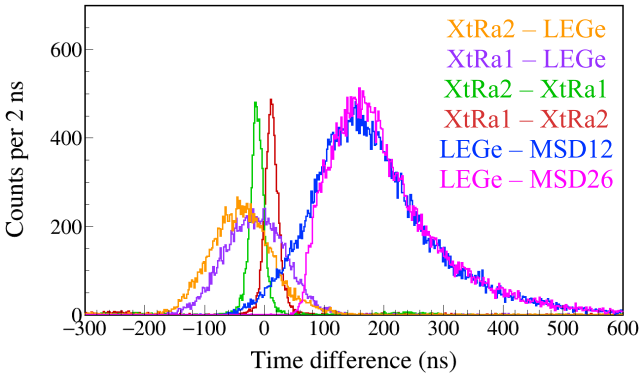

FIG. 16. Coincidence time spectra between each detector. From left to right: the six time peaks correspond to three decay sequences: the ^{152}Eu 40−46-keV and 1408-keV X-γ coincidences measured by XtRa-LEGe, the ^{60}Co 1173-keV and 1332-keV γ-γ coincidences measured by XtRa-XtRa, and the ^{241}Am 5486-keV and 59.5-keV α-γ coincidences measured by LEGe-MSD. In each decay sequence, the timestamp of the prior event is subtracted from the timestamp of the subsequent event.

VI. CALCULATIONS & SIMULATIONS

To assess the feasibility of observables in future the ^{60}Ga decay measurement with PXCT, we performed shell-model calculations in the truncated fp-shell model space with the GPFX1A Hamiltonian [125] using the NuShellX@MSU code [126]. The newly-evaluated ^{60}Ga $Q_{\rm EC}$ = 14161(15) keV was incorporated into the calculation. We obtained 900 ^{60}Zn states populated by ^{60}Ga decay up to E_x = 12.6 MeV, with 300 states each for $J^\pi = 1^+, 2^+, 3^+$. A quenching factor $q^2 = 0.6$ for the matrix elements of the Gamow-Teller operator was used to calculate the β feedings in ^{60}Ga decay. We calculated the decay widths Γ_γ and Γ_p for 128 resonances with $J^\pi = 0^+, 1^+, 2^+, 3^+, 4^+, 5^+$ up to the ^{59}Cu(p,α) Gamow window at 1.5 GK. We also calculated the average decay widths Γ_γ, Γ_p, and Γ_α using the statistical model code NON-SMOKER [8]. We adopted the shell-model calculated Γ_γ and Γ_p and the statistical-model calculated Γ_α to calculate the ^{59}Cu$(p,\gamma)^{60}$Zn and ^{59}Cu$(p,\alpha)^{56}$Ni reaction rates by combining all 128 positive parity resonances. The fractional contributions of each resonance are shown in Fig. 18. The statistical model calculation indicates that the level densities for 1^- and 2^- states in ^{60}Zn fall below 1 MeV^{-1} at excitation energies of 7.2 and 6.9 MeV, respectively. This suggests that $\ell = 0$ resonances are less likely to be present within the Gamow window and to significantly contribute to the total reaction rate. Table V summarizes the properties of the six most influential ^{59}Cu$(p,\gamma)^{60}$Zn resonances. It should be noted that the uncertainties of the shell-model calculated excitation/resonance energies typically range from 200 keV to 500 keV for this mass region. The resonances listed in Table V are not the specific resonances that our experiment aims to identify but rather represent a typical potential scenario that we may encounter. Any ^{60}Zn resonances that we are able to identify through ^{60}Ga β decay may help constrain the ^{59}Cu$(p,\gamma)^{60}$Zn and ^{59}Cu$(p,\alpha)^{56}$Ni reaction rates.

A statistically meaningful reaction rate calculation with principled uncertainty quantification will be discussed in a forthcoming paper [127], in which all the nuclear physics properties entering into the reaction rate calculation are randomly sampled according to appropriate probability density functions [128–132].

One of the key observables offered by our experimental setup is the proton-X-ray coincidences. We conducted GEANT4 simulation incorporating the theoretical ^{60}Ga decay scheme and the known decay schemes of the daughter nuclei [35–37], the detector responses characterized based on radioactive source tests, and the projected statistics over a 20-day period with a 9×10^3 pps

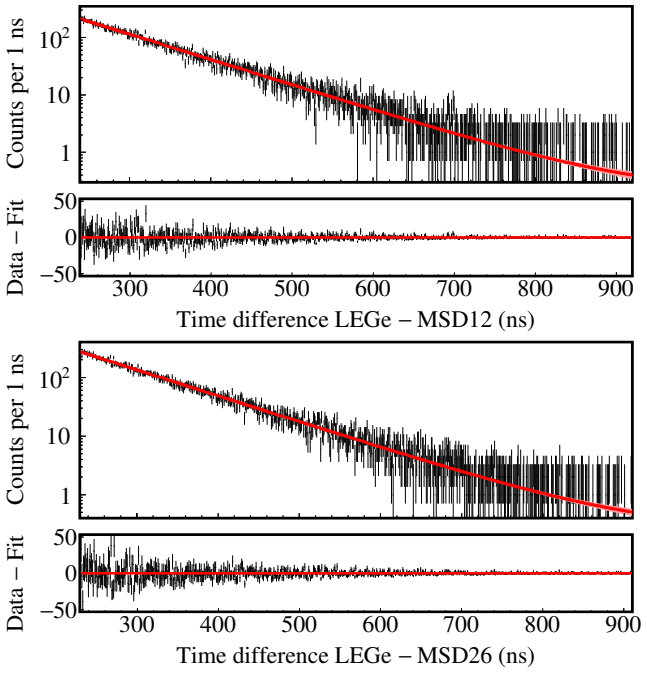

FIG. 17. Time differences between the 59.5-keV γ-ray signals in LEGe and the 5486-keV α signals in the MSD silicon detector telescope. From the fit, we obtain the $T_{1/2}$ = 68.1(6) ms, p-value = 0.34, and χ^2_ν = 1.02 by dividing the χ^2 value by the number of degrees of freedom, from LEGe-MSD12, and $T_{1/2}$ = 67.9(5) ms, p-value = 0.88, and χ^2_ν = 0.94 from LEGe-MSD26.

TABLE V. Properties of potentially important ^{59}Cu$(p,\gamma)^{60}$Zn resonances predicted by the shell model. The values in the first through tenth columns represent the spin and parity (J^π), excitation energy (E_x), resonance energy (E_r), partial decay widths (Γ_γ, Γ_p, Γ_α), lifetime (τ), log ft value and β-feeding intensity (I_β) for ^{60}Ga decay, and ratio of EC/β+ feeding [46].

J^π	E_x (keV)	E_r (keV)	Γ_γ (eV)	Γ_p (eV)	Γ_α (eV)[a]	τ (fs)	log ft	I_β (%)	$R_{\mathrm{EC}/\beta+}$
2^+	5501	396	3.8×10^{-2}	7.4×10^{-10}	2.9×10^{-7}	17.3	5.463	0.314	1.6×10^{-3}
1^+	5566	461	6.4×10^{-2}	1.5×10^{-7}	0	10.3	4.708	1.713	1.6×10^{-3}
2^+	5645	540	1.9×10^{-1}	2.1×10^{-6}	1.1×10^{-6}	3.5	6.146	0.060	1.7×10^{-3}
2^+	5989	884	3.3×10^{-2}	4.7×10^{-3}	1.6×10^{-5}	17.5	5.367	0.287	1.9×10^{-3}
2^+	6072	967	2.5×10^{-1}	5.7×10^{-2}	2.9×10^{-5}	2.1	5.536	0.184	2.0×10^{-3}
1^+	6305	1200	2.0×10^{-1}	2.1×10^{-1}	1.3×10^{-27}	1.6	7.035	0.005	2.2×10^{-3}

[a] From the statistical model calculation.

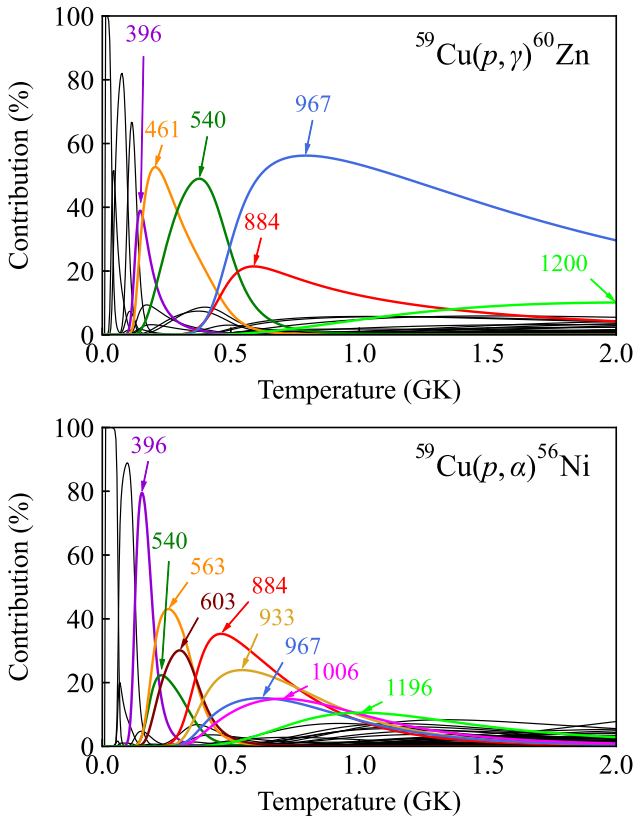

FIG. 18. Fractional contributions of 128 shell-model predicted resonances to the ^{59}Cu$(p,\gamma)^{60}$Zn (upper) and ^{59}Cu$(p,\alpha)^{56}$Ni (lower) reaction rates. The most influential resonances are labeled with their corresponding resonance energies in keV.

^{60}Ga beam. The resulting simulated proton and α particle identification spectrum by the ΔE-E telescope and proton-gated X-ray spectrum by LEGe are shown in Fig. 19.

The Cu/Zn K_α X-ray count ratio can be determined by integrating the 8.0- and 8.6-keV X-ray peaks observed in coincidence with protons. The Zn K_α radiative transition probability is 41.7%, compared to 38.7% for Cu [47], and the LEGe detection efficiency for 8.6-keV photons is 7.8%, compared to 7.4% at 8.0 keV (Fig. 8). Consequently, we need to apply two correction factors of $F = 1.07$ for fluorescence yields and $E = 1.05$ for efficiencies when extracting the lifetime of the proton-emitting state in ^{60}Zn from the observed Cu/Zn K_α X-ray count ratio:

$$\tau_{p-\mathrm{emit}} = \frac{\tau_{K\mathrm{shell(Zn)}}}{R_{\mathrm{Cu/Zn}}}, \tag{11}$$

$$R_{\mathrm{Cu/Zn}} = \frac{I_{K_\alpha(\mathrm{Cu})}\times F\times E}{I_{K_\alpha(\mathrm{Zn})}}, \tag{12}$$

The uncertainty in the inferred lifetime will likely be dominated by statistical uncertainty. The main source of systematic uncertainty is the recommended Zn K-shell vacancy width $\Gamma_{K\mathrm{shell(Zn)}} = 1.62$ eV [51], adjusted based on the calculated $\Gamma_{K\mathrm{shell(Zn)}} = 1.56$ eV from Ref. [47]. A resonant Raman scattering measurement reported $\Gamma_{K\mathrm{shell(Zn)}} = 1.9(1)$ eV [133], which is consistent with the recommended value, considering estimated uncertainty of 5−25% for atomic numbers below 30 [51].

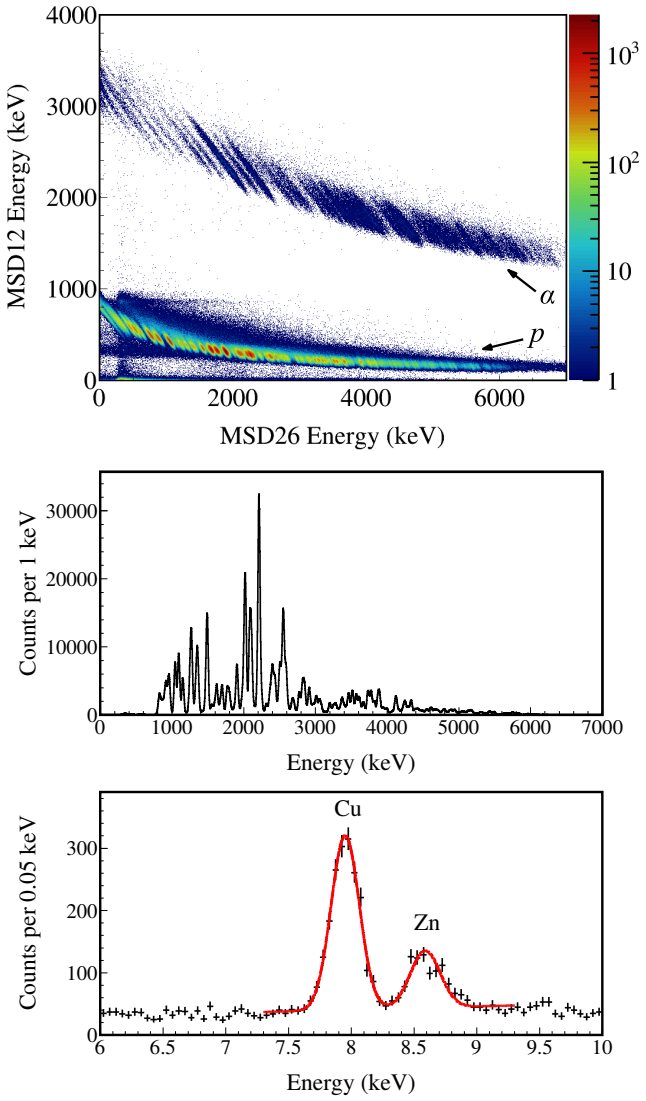

FIG. 19. Top panel: simulated charged-particle ΔE-E spectrum by taking into the theoretical decay properties of ^{60}Ga and the measured detector responses. Middle panel: ^{60}Ga EC/β^+-delayed proton energy spectrum selected from the ΔE-E plot. Bottom panel: the X-ray spectrum gated by all protons in the ΔE-E spectrum, which yields a total X ratio of $R_{\mathrm{Zn/Cu}} = 0.31(3)$. A double-Gaussian fit is superimposed on the Cu and Zn K_α peaks.

VII. SUMMARY & OUTLOOK

We present the design, construction, simulation, and radioactive source testing of the PXCT detection system. The system is capable of detecting all types of charged particles and photons emitted in the EC/β^+ decay, which will enable us to measure the decay branching ratios for proton, α, γ rays, and the lifetimes of resonances. Proton/α/γ coincidences will offer information on the proton/α-emitting states in the compound nucleus and the ground and excited states of daughter nuclei, pertinent to both the entrance and exit channels for particle-induced reactions. Statistical analysis of the PXCT data can provide the nuclear level density and transmission coefficients needed for calculating reaction rates using the Hauser-Feshbach statistical model. The application of PXCT to 60Ga EC/β^+ decay offers the unique advantage of obtaining all necessary quantities required for the ^{59}Cu$(p,\gamma)^{60}$Zn and ^{59}Cu$(p,\alpha)^{56}$Ni thermonuclear reaction rate calculations in a single experiment. This approach eliminates the need for separate indirect measurements of different quantities, thereby enhancing the accuracy and consistency of astrophysically relevant nuclear data.

The PXCT system holds great potential for studying other important reaction rates in the *rp*-process. As shown in Fig. 1, ^{64}Ge plays an analogous role in the ZnGa cycle to that of ^{60}Zn in the NiCu cycle [18, 19, 134]. One difference is that the allowed β transitions of the 0^+ ^{64}As ground state populate the 0^+ and 1^+ states in ^{64}Ge [71]. Given the comparable Q_{EC}, half-lives, proton/α-separation energies, and key X-ray energies (Table III), it is technically possible to extend this method to study the EC/β^+ decay of ^{64}As to address the competition between the ^{63}Ga$(p,\gamma)^{64}$Ge and ^{63}Ga$(p,\alpha)^{60}$Zn reactions.

VIII. ACKNOWLEDGMENTS

We gratefully acknowledge Stephen Gillespie, Aaron Chester, Giordano Cerizza, and the FRIB Mechanical Engineering Department for their technical assistance. We would like to thank Jun Chen for the helpful discussions. This work was supported by the U.S. National Science Foundation under Grants Nos. PHY-1913554, PHY-2110365, and PHY-2209429, and the U.S. Department of Energy, Office of Science, under Awards Nos. DE-SC0016052 and DE-SC0023529.

[1] M. Aliotta, R. Buompane, M. Couder, A. Couture, R. J. deBoer, A. Formicola, L. Gialanella, J. Glorius, G. Imbriani, M. Junker, J. Phys. G: Nucl. Part. Phys. **49**, 010501 (2022).

[2] R. E. Tribble, C. A. Bertulani, M. La Cognata, A. M. Mukhamedzhanov, and C. Spitaleri, Rep. Prog. Phys. **77**, 106901 (2014).

[3] C. R. Brune and B. Davids, Annu. Rev. Nucl. Part. Sci. **65**, 87 (2015).

[4] Faïrouz Hammache and Nicolas de Séréville, Front. Phys. **8**, 602920 (2021).
[5] C. Angulo, M. Arnould, M. Rayet, P. Descouvemont, D. Baye, C. Leclercq-Willain, A. Coc, S. Barhoumi, P. Aguer, C. Rolfs, R. Kunz, J. W. Hammer, A. Mayer, T. Paradellis, S. Kossionides, C. Chronidou, K. Spyrou, S. Degl'Innocenti, G. Fiorentini, B. Ricci, S. Zavatarelli, C. Providencia, H. Wolters, J. Soares, C. Grama, J. Rahighi, A. Shotter, and M. Lamehi Rachti, Nucl. Phys. A **656**, 3 (1999).
[6] C. E. Rolfs and W. S. Rodney, *Cauldrons in the Cosmos*, University of Chicago Press, Chicago, USA (1988).
[7] C. Iliadis, *Nuclear Physics of Stars*, Wiley-VCH, Verlag, Wenheim, Germany (2015).
[8] T. Rauscher and F. K. Thielemann, At. Data Nucl. Data Tables **75**, 1 (2000).
[9] T. Rauscher, *Essentials of Nucleosynthesis and Theoretical Nuclear Astrophysics*, IOP Publishing, Bristol, UK (2020).
[10] J. C. Hardy, J. A. Macdonald, H. Schmeing, H. R. Andrews, J. S. Geiger, R. L. Graham, T. Faestermann, E. T. H. Clifford, and K. P. Jackson, Phys. Rev. Lett. **37**, 133 (1976).
[11] J. José, *Stellar Explosions: Hydrodynamics and Nucleosynthesis*, CRC Press, Boca Raton, USA (2016).
[12] H. Schatz and K. E. Rehm, Nucl. Phys. A **777**, 601 (2006).
[13] A. Parikh, J. José, G. Sala, and C. Iliadis, Prog. Part. Nucl. Phys. **69**, 225 (2013).
[14] L. van Wormer, J. Görres, C. Iliadis, M. Wiescher, and F.-K. Thielemann, Astrophys. J. **432**, 326 (1994).
[15] Richard H. Cyburt, A. Matthew Amthor, Ryan Ferguson, Zach Meisel, Karl Smith, Scott Warren, Alexander Heger, R. D. Hoffman, Thomas Rauscher, Alexander Sakharuk, Hendrik Schatz, F. K. Thielemann, Michael Wiescher, Astrophys. J. Suppl. Ser. **189**, 240 (2010).
[16] T. Rauscher and F. K. Thielemann, At. Data Nucl. Data Tables **79**, 47 (2001).
[17] A. Parikh, J. José, F. Moreno, and C. Iliadis, Astrophys. J. Suppl. Ser. **178**, 110 (2008).
[18] R. H. Cyburt, A. M. Amthor, A. Heger, E. Johnson, L. Keek, Z. Meisel, H. Schatz, and K. Smith, Astrophys. J. **830**, 55 (2016).
[19] Zach Meisel, Grant Merz, and Sophia Medvid, Astrophys. J. **872**, 84 (2019).
[20] C. Fröhlich, G. Martínez-Pinedo, M. Liebendörfer, F.-K. Thielemann, E. Bravo, W. R. Hix, K. Langanke, and N. T. Zinner, Phys. Rev. Lett. **96**, 142502 (2006).
[21] A. Arcones, C. Fröhlich, and G. Martínez-Pinedo, Astrophys. J. **750**, 18 (2012).
[22] Kirby Hermansen, Sean M. Couch, Luke F. Roberts, Hendrik Schatz, MacKenzie L. Warren, Astrophys. J. **901**, 77 (2020).
[23] J. S. Randhawa, R. Kanungo, J. Refsgaard, P. Mohr, T. Ahn, M. Alcorta, C. Andreoiu, S. S. Bhattacharjee, B. Davids, G. Christian, A. A. Chen, R. Coleman, P. E. Garrett, G. F. Grinyer, E. Gyabeng Fuakye, G. Hackman, J. Hollett, R. Jain, K. Kapoor, R. Krücken, A. Laffoley, A. Lennarz, J. Liang, Z. Meisel, B. Nikhil, A. Psaltis, A. Radich, M. Rocchini, N. Saei, M. Saxena, M. Singh, C. Svensson, P. Subramaniam, A. Talebitaher, S. Upadhyayula, C. Waterfield, J. Williams, and M. Williams, Phys. Rev. C **104**, L042801 (2021).
[24] D. Soltesz, M. A. A. Mamun, A. V. Voinov, Z. Meisel, B. A. Brown, C. R. Brune, S. M. Grimes, H. Hadizadeh, M. Hornish, T. N. Massey, J. E. O'Donnell, and W. E. Ormand, Phys. Rev. C **103**, 015802 (2021).
[25] Chanhee Kim, Kyungyuk Chae, Soomi Cha, Kyujin Kwak, Gwangeon Seong, and Michael Smith, Astrophys. J. **929**, 96 (2022).
[26] Konrad Schmidt, NSCL Experiment 18039.
[27] Melina Avila, FRIB Experiment 21026.
[28] Gavin Lotay, FRIB Experiment 21014.
[29] Zach Meisel, NSCL Experiment 17009.
[30] Chris Wrede, FRIB Experiment 23035.
[31] T. Rauscher, Phys. Rev. C **81**, 045807 (2010).
[32] M. Wang, W. J. Huang, F. G. Kondev, G. Audi, S. Naimi, Chin. Phys. C **45**, 030003 (2021).
[33] S. E. A. Orrigo, B. Rubio, W. Gelletly, P. Aguilera, A. Algora, A. I. Morales, J. Agramunt, D. S. Ahn, P. Ascher, B. Blank, C. Borcea, A. Boso, R. B. Cakirli, J. Chiba, G. de Angelis, G. de France, F. Diel, P. Doornenbal, Y. Fujita, N. Fukuda, E. Ganioğlu, M. Gerbaux, J. Giovinazzo, S. Go, T. Goigoux, S. Grévy, V. Guadilla, N. Inabe, G. G. Kiss, T. Kubo, S. Kubono, T. Kurtukian-Nieto, D. Lubos, C. Magron, F. Molina, A. Montaner-Pizá, D. Napoli, D. Nishimura, S. Nishimura, H. Oikawa, V. H. Phong, H. Sakurai, Y. Shimizu, C. Sidong, P.-A. Söderström, T. Sumikama, H. Suzuki, H. Takeda, Y. Takei, M. Tanaka, J. Wu, and S. Yagi, Phys. Rev. C **103**, 014324 (2021).
[34] S. F. Paul, J. Bergmann, J. D. Cardona, K. A. Dietrich, E. Dunling, Z. Hockenbery, C. Hornung, C. Izzo, A. Jacobs, A. Javaji, B. Kootte, Y. Lan, E. Leistenschneider, E. M. Lykiardopoulou, I. Mukul, T. Murböck, W. S. Porter, R. Silwal, M. B. Smith, J. Ringuette, T. Brunner, T. Dickel, I. Dillmann, G. Gwinner, M. MacCormick, M. P. Reiter, H. Schatz, N. A. Smirnova, J. Dilling, and A. A. Kwiatkowski, Phys. Rev. C **104**, 065803 (2021).
[35] Huo Junde, Huo Su, Yang Dong, Nucl. Data Sheets **112**, 1513 (2011).
[36] M. Shamsuzzoha Basunia, Nucl. Data Sheets **151**, 1 (2018).
[37] E. Browne and J. K. Tuli, Nucl. Data Sheets **114**, 1849 (2013).
[38] C. Mazzocchi, Z. Janas, J. Döring, M. Axiotis, L. Batist, R. Borcea, D. Cano-Ott, E. Caurier, G. de Angelis, E. Farnea, A. Faßbender, A. Gadea, H. Grawe, A. Jungclaus, M. Kapica, R. Kirchner, J. Kurcewicz, S.M. Lenzi, T. Martínez, I. Mukha, E. Nácher, D. R. Napoli, E. Roeckl, B. Rubio, R. Schwengner, J. L. Tain, and C. A. Ur, Eur. Phys. J. A **12**, 269 (2001).
[39] M. J. López Jiménez, B. Blank, M. Chartier, S. Czajkowski, P. Dessagne, G. de France, J. Giovinazzo, D. Karamanis, M. Lewitowicz, V. Maslov, C. Miehé, P. H. Regan, M. Stanoiu, and M. Wiescher, Phys. Rev. C **66**, 025803 (2002).
[40] L. Kucuk, S. E. A. Orrigo, A. Montaner-Pizá, B. Rubio, Y. Fujita, W. Gelletly, B. Blank, Y. Oktem, T. Adachi, A. Algora, P. Ascher, R. B. Cakirli, G. de France, H. Fujita, E. Ganioğlu, J. Giovinazzo, S. Grévy, F. M. Marqués, F. Molina, F. de Oliveira Santos, L. Perrot, R. Raabe, P. C. Srivastava, G. Susoy, A. Tamii, J. C Thomas, Eur. Phys. J. A **53**, 134 (2017).

[41] Thomas Goigoux, Ph.D. Thesis, Université de Bordeaux, Gradignan, France, 2017.

[42] J. Giovinazzo, T. Goigoux, B. Blank, P. Ascher, M. Gerbaux, S. Grévy, T. Kurtukian-Nieto, C. Magron, P. Doornenbal, N. Fukuda, N. Inabe, G.G. Kiss, T. Kubo, S. Kubono, S. Nishimura, H. Sakurai, Y. Shimizu, C. Sidong, P.-A. Söderström, T. Sumikama, H. Suzuki, H. Takeda, P. Vi, J. Wu, D.S. Ahn, J. Agramunt, A. Algora, V. Guadilla, A. Montaner-Piza, A.I. Morales, S.E.A. Orrigo, B. Rubio, Y. Fujita, M. Tanaka, W. Gelletly, P. Aguilera, F. Molina, F. Diel, D. Lubos, G. de Angelis, D. Napoli, C. Borcea, A. Boso, R.B. Cakirli, E. Ganioglu, J. Chiba, D. Nishimura, H. Oikawa, Y. Takei, S. Yagi, K. Wimmer, G. de France, S. Go, B.A. Brown, Acta Phys. Pol. B **51**, 577 (2020).

[43] J. Chen, ENSDF Analysis and Utility Programs, Gamma to Level Scheme Computation.

[44] R. Kamermans, H. W. Jongsma, J. van der Spek, and H. Verheul, Phys. Rev. C **10**, 620 (1974).

[45] Carl Svensson, Ph.D. Thesis, McMaster University, Ontario, Canada, 1998.

[46] J. Chen, ENSDF Analysis and Utility Programs, Radiation Report.

[47] S. T. Perkins, D. E. Cullen, M.-H. Chen, J. H. Hubbell, J. Rathkopf, and J. H. Scofield, LLNL Evaluated Atomic Data Library (EADL), Tech. Rep. UCRL-50400 **30** (1991).

[48] W. Bambynek, B. Crasemann, R. W. Fink, H. U. Freund, H. Mark, C. D. Swift, R. E. Price, and P. Venugopala Rao, Rev. Mod. Phys. **44**, 716 (1972).

[49] J. H. Scofield, Chap. 6 Radiative Transitions in *Atomic Inner-Shell Processes*, B. Crasemann ed., Academic Press: New York, USA, 1975).

[50] Karol Kozioł, Phys. Rev. A **89**, 022515 (2014).

[51] J. L. Campbell and T. Papp, At. Data Nucl. Data Tables **77**, 1 (2001).

[52] P. J. Nolan and J. F. Sharpey-Schafer, Rep. Prog. Phys. **42**, 1 (1979).

[53] E. Browne, J.K. Tuli, Nucl. Data Sheets **111**, 2425 (2010).

[54] J. Giovinazzo, Ph. Dessagne, and Ch. Miehé, Nucl. Phys. A **674**, 394 (2000).

[55] J.C. Hardy, J.A. MacDonald, H. Schmeing, T. Faestermann, H.R. Andrews, J.S. Geiger, R.L. Graham, K.P. Jackson, Phys. Lett. B **63**, 27 (1976).

[56] K. Vierinen, Nucl. Phys. A **463**, 605 (1987).

[57] J.C. Hardy, T. Faestermann, H. Schmeing, J.A. Macdonald, H.R. Andrews, J.S. Geiger, R.L. Graham, and K.P. Jackson, Nucl. Phys. A **371**, 349 (1981).

[58] C.D. Nesaraja, Nucl. Data Sheets **115**, 1 (2014).

[59] J. A. Macdonald, J. C. Hardy, H. Schmeing, T. Faestermann, H. R. Andrews, J. S. Geiger, R. L. Graham, and K. P. Jackson, Nucl. Phys. A **288**, 1 (1977).

[60] Ph. Dessagne, Ch. Miehé, P. Baumann, A. Huck, G. Klotz, M. Ramdane, G. Walter, and J. M. Maison, Phys. Rev. C **37**, 2687 (1988).

[61] B. Singh and J. Chen, Nucl. Data Sheets **158**, 1 (2019).

[62] P. Hornshøj, K.Wilsky, P.G.Hansen, and B.Jonson, Nucl. Phys. A **187**, 637 (1972).

[63] Ch. Miehé, Ph. Dessagne, Ch. Pujol, G. Walter, B. Jonson, and M. Lindroos, Eur. Phys. J. A **5**, 143 (1999).

[64] P. Asboe-Hansen, E. Hagberg, P. G. Hansen, J. C. Hardy, P. Hornshøj, B. Jonson, S. Mattsson, P. Tidemand-Petersson, Phys. Lett. B **77**, 363 (1978).

[65] P. Asboe-Hansen, E. Hagberg, P. G. Hansen, J. C. Hardy, B. Jonson, and S. Mattsson, Nucl. Phys. A **361**, 23 (1981).

[66] B. Singh and N. Nica, Nucl. Data Sheets **113**, 1115 (2012).

[67] Jean Blachot, Nucl. Data Sheets **111**, 1471 (2010).

[68] Z. Janas, L. Batist, R. Borcea, J. Döring, M. Gierlik, M. Karny, R. Kirchner, M. La Commara, S. Mandal, C. Mazzocchi, F. Moroz, S. Orlov, A. Płochocki, E. Roeckl, and J. Żylicz, Eur. Phys. J. A **24**, 205 (2005).

[69] Jean Blachot, Nucl. Data Sheets **95**, 679 (2002).

[70] Z. Janas, L. Batist, J. Döring, M. Gierlik, R. Kirchner, J. Kurcewicz, H. Mahmud, C. Mazzocchi, A. Płochocki, E. Roeckl, K. Schmidt, P. J. Woods, and J. Żylicz, Eur. Phys. J. A **23**, 401 (2005).

[71] Balraj Singh and Jun Chen, Nucl. Data Sheets **178**, 41 (2021).

[72] X. Zhou, M. Wang, Y. H. Zhang, Yu. A. Litvinov, Z. Meisel, K. Blaum, X. H. Zhou, S. Q. Hou, K. A. Li, H. S. Xu, R. J. Chen, H. Y. Deng, C. Y. Fu, W. W. Ge, J. J. He, W. J. Huang, H. Y. Jiao, H. F. Li, J. G. Li, T. Liao, A. Litvinov, M. L. Liu, Y. F. Niu, P. Shuai, J. Y. Shi, Y. N. Song, M. Z. Sun, Q. Wang, Y. M. Xing, X. Xu, F. R. Xu, X. L. Yan, J. C. Yang, Y. Yu, Q. Yuan, Y. J. Yuan, Q. Zeng, M. Zhang, and S. Zhang, Nat. Phys. **19**, 1091 (2023).

[73] B. Rubio, P. Aguilera, F. Molina, J. Agramunt, A. Algora, V. Guadilla, A. Montaner-Pizá, A. I. Morales, S. E. A. Orrigo, W. Gelletly, B. Blank, P. Asher, M. Gerbaux, J. Giovinazzo, S. Grevy, T. Kurtukian, C. Magron, J. Chiba, D. Nishimura, H. Oikawa, Y. Takei, S. Yang, D. S. Ahn, P. Doornenbal, N. Fukuda, N. Inabe, G. Kiss, T. Kubo, S. Kubono, S. Nishimura, Y. Shimizu, C. Sidong, P.-A. Söderström, T. Sumikama, H. Suzuki, H. Takeda, P. Vi, J. Wu, Y. Fujita, M. Tanaka, F. Diel, D. Lubos, G. de Angelis, D. Napoli, C. Borcea, A. Boso, R. B. Cakirli, E. Ganioglu, G. de France, S. Go, J. Phys.: Conf. Ser. **1308**, 012018 (2019).

[74] A. Gilbert and A. G. W. Cameron, Can. J. Phys. **43**, 1446 (1965).

[75] W. Dilg, W. Schantl, H. Vonach, and M. Uhl, Nucl. Phys. A **217**, 269 (1973).

[76] J. Wei, H. Ao, B. Arend, S. Beher, G. Bollen, N. Bultman, F. Casagrande, W. Chang, Y. Choi, S. Cogan, C. Compton, M. Cortesi, J. Curtin, K. Davidson, X. Du, K. Elliott, B. Ewert, A. Facco, A. Fila, K. Fukushima, V. Ganni, A. Ganshyn, J. Gao, T. Glasmacher, J. Guo, Y. Hao, W. Hartung, N. Hasan, M. Hausmann, K. Holland, H. C. Hseuh, M. Ikegami, D. Jager, S. Jones, N. Joseph, T. Kanemura, S.-H. Kim, P. Knudsen, B. Kortum, E. Kwan, T. Larter, R. E. Laxdal, M. Larmann, K. Laturkar, J. LeTourneau, Z.-Y. Li, S. Lidia, G. Machicoane, C. Magsig, P. Manwiller, F. Marti, T. Maruta, A. McCartney, E. Metzgar, S. Miller, Y. Momozaki, D. Morris, M. Mugerian, I. Nesterenko, C. Nguyen, W. O'Brien, K. Openlander, P. N. Ostroumov, M. Patil, A. S. Plastun, J. Popielarski, L. Popielarski, M. Portillo, J. Priller, X. Rao, M. Reaume, H. Ren, K. Saito, M. Smith, M. Steiner, A. Stolz, O. B. Tarasov, B. Tousignant, R. Walker, X. Wang, J. Wenstrom, G. West, K. Witgen, M. Wright, T. Xu, Y. Xu, Y. Yamazaki, T. Zhang, Q. Zhao, S. Zhao, K. Dixon, M. Wiseman, M. Kelly, K. Hosoyama, and S.

Prestemon, Mod. Phys. Lett. A **37**, 2230006 (2022).
[77] M. Portillo, B.M. Sherrill, Y. Choi, M. Cortesi, K. Fukushima, M. Hausmann, E. Kwan, S. Lidia, P.N. Ostroumov, R. Ringle, M.K. Smith, M. Steiner, O.B. Tarasov, A.C.C. Villari, and T. Zhang, Nucl. Instrum. Methods Phys. Res. B **540**, 151 (2023).
[78] C.S. Sumithrarachchi, D.J. Morrissey, S. Schwarz, K. Lund, G. Bollen, R. Ringle, G. Savard, and A.C.C. Villari, Nucl. Instrum. Methods Phys. Res. B **463**, 305 (2020).
[79] K.R. Lund, G. Bollen, D. Lawton, D.J. Morrissey, J. Ottarson, R. Ringle, S. Schwarz, C.S. Sumithrarachchi, A.C.C. Villari, and J. Yurkon, Nucl. Instrum. Methods Phys. Res. B **463**, 378 (2020).
[80] A.C.C. Villari, G. Bollen, A. Henriques, A. Lapierre, S. Nash, R. Ringle, S. Schwarz, C.S. Sumithrarachchi, Nucl. Instrum. Methods Phys. Res. B **541**, 350 (2023).
[81] J. F. Ziegler, M. D.Ziegler, and J. P. Biersack, Nucl. Instrum. Methods Phys. Res. B **268**, 1818 (2010).
[82] MIRION Low Energy Germanium Detector.
[83] MIRION Extended Range Coaxial Germanium Detector.
[84] MIRION Cryo-Pulse 5 PLUS Electrically Refrigerated Cryostat.
[85] D. Willems, R. Arts, B.V.-J. Douwen, MIRION Technical Paper (2015).
[86] MIRCON MSD12 Circular Silicon Detector.
[87] MIRCON MSD26 Circular Silicon Detector.
[88] MIRION Intelligent Preamplifier.
[89] J. Eberth, H. Hess, P. Reiter, S. Bertoldo, C. Carraro, G. Maggioni, D. R. Napoli, W. Raniero, and D. De Salvador, Eur. Phys. J. A **59**, 179 (2023).
[90] ORTEC 660 Dual 5-kV Bias Supply.
[91] Mesytec MPR-1 Charge Integrating Preamplifier.
[92] Mesytec MHV-4 High Voltage Supply.
[93] Mesytec MNV-4 NIM Power Supply.
[94] XIA Pixie-16 Digitizer.
[95] K. Starosta, C. Vaman, D. Miller, P. Voss, D. Bazin, T. Glasmacher, H. Crawford, P. Mantica, H. Tan, W. Hennig, M. Walby, A. Fallu-Labruyere, J. Harris, D. Breus, P. Grudberg, W.K. Warburton, Nucl. Instrum. Methods Phys. Res. A **610**, 700 (2009).
[96] C.J. Prokop, S.N. Liddick, B.L. Abromeit, A.T. Chemey, N.R. Larson, S. Suchyta, J.R. Tompkins, Nucl. Instrum. Methods Phys. Res. A **741**, 163 (2014).
[97] XIA Pixie-16 Digitizer User Manual.
[98] H.Y. Wu, Z.H. Li, H. Tan, H. Hua, J. Li, W. Hennig, W.K. Warburton, D.W. Luo, X. Wang, X.Q. Li, S.Q. Zhang, C. Xu, Z.Q. Chen, C.G. Wu, Y. Jin, J. Lin, D.X. Jiang, Y.L. Ye, Nucl. Instrum. Methods Phys. Res. A **975**, 164200 (2020).
[99] D. Weisshaar, D. Bazin, P.C. Bender, C.M. Campbell, F. Recchia, V. Bader, T. Baugher, J. Belarge, M.P. Carpenter, H.L. Crawford, M. Cromaz, B. Elman, P. Fallon, A. Forney, A. Gade, J. Harker, N. Kobayashi, C. Langer, T. Lauritsen, I.Y. Lee, A. Lemasson, B. Longfellow, E. Lunderberg, A.O. Macchiavelli, K. Miki, S. Momiyama, S. Noji, D.C. Radford, M. Scott, J. Sethi, S.R. Stroberg, C. Sullivan, R. Titus, A. Wiens, S. Williams, K. Wimmer, S. Zhu, Nucl. Instrum. Methods Phys. Res. A **847**, 187 (2017).
[100] BNC Model DB-2 NIM Random Pulse Generator.
[101] Y. Isozumi, Nucl. Instrum. Methods Phys. Res. A **280**, 151 (1989).
[102] M. S. Rapaport, F. Asaro, and I. Perlman, Phys. Rev. C **11**, 1740 (1975).
[103] Juhani Kantele, *Handbook of Nuclear Spectrometry*, Academic Press, London (1995).
[104] L. J. Sun, M. Friedman, T. Budner, D. Pérez-Loureiro, E. Pollacco, C. Wrede, B. A. Brown, M. Cortesi, C. Fry, B. E. Glassman, J. Heideman, M. Janasik, A. Kruskie, A. Magilligan, M. Roosa, J. Stomps, J. Surbrook, and P. Tiwari, Phys. Rev. C **103**, 014322 (2021).
[105] Matt Newville, easyXAFS, Matteo Levantino, Christian Schlepuetz, Damian Günzing, Max Rakitin, Sang-Woo Kim, and kalvdans, xraypy/XrayDB: (4.5.1). Zenodo (2023).
[106] M. Basunia, Nucl. Data Sheets **107**, 2323 (2006).
[107] M.-M. Bé, V. Chisté, C. Dulieu, X. Mougeot, E. Browne, V. Chechev, N. Kuzmenko, F. Kondev, A. Luca, M. Galán, A.L. Nichols, A. Arinc, and X. Huang, Mono. BIPM-5 - Table of Radionuclides, Vol.2 (2004).
[108] Devinder Mehta, M.L. Garg, Jasbir Singh, Nirmal Singh, T.S. Cheema, P.N. Trehan, Nucl. Instrum. Methods Phys. Res. A **245**, 447 (1986).
[109] M.-M. Bé, V. Chisté, C. Dulieu, X. Mougeot, E. Browne, V. Chechev, N. Kuzmenko, F. Kondev, A. Luca, M. Galán, A.L. Nichols, A. Arinc, and X. Huang, Mono. BIPM-5 - Table of Radionuclides, Vol.5 (2010).
[110] S. Agostinelli, J. Allison, K. Amako, J. Apostolakis, H. Araujo, P. Arce, M. Asai, D. Axen, S. Banerjee, G. Barrand, F. Behner, L. Bellagamba, J. Boudreau, L. Broglia, A. Brunengo, H. Burkhardt, S. Chauvie, J. Chuma, R. Chytracek, G. Cooperman, G. Cosmo, P. Degtyarenko, A. Dell'Acqua, G. Depaola, D. Dietrich, R. Enami, A. Feliciello, C. Ferguson, H. Fesefeldt, G. Folger, F. Foppiano, A. Forti, S. Garelli, S. Giani, R. Giannitrapani, D. Gibin, J. J. Gómez Cadenas, I. González, G. Gracia Abril, G. Greeniaus, W. Greiner, V. Grichine, A. Grossheim, S. Guatelli, P. Gumplinger, R. Hamatsu, K. Hashimoto, H. Hasui, A. Heikkinen, A. Howard, V. Ivanchenko, A. Johnson, F. W. Jones, J. Kallenbach, N. Kanaya, M. Kawabata, Y. Kawabata, M. Kawaguti, S. Kelner, P. Kent, A. Kimura, T. Kodama, R. Kokoulin, M. Kossov, H. Kurashige, E. Lamanna, T. Lampén, V. Lara, V. Lefebure, F. Lei, M. Liendl, W. Lockman, F. Longo, S. Magni, M. Maire, E. Medernach, K. Minamimoto, P. Mora de Freitas, Y. Morita, K. Murakami, M. Nagamatu, R. Nartallo, P. Nieminen, T. Nishimura, K. Ohtsubo, M. Okamura, S. O'Neale, Y. Oohata, K. Paech, J. Perl, A. Pfeiffer, M. G. Pia, F. Ranjard, A. Rybin, S. Sadilov, E. Di Salvo, G. Santin, T. Sasaki, N. Savvas, Y. Sawada, S. Scherer, S. Sei, V. Sirotenko, D. Smith, N. Starkov, H. Stoecker, J. Sulkimo, M. Takahata, S. Tanaka, E. Tcherniaev, E. Safai Tehrani, M. Tropeano, P. Truscott, H. Uno, L. Urban, P. Urban, M. Verderi, A. Walkden, W. Wander, H. Weber, J. P. Wellisch, T. Wenaus, D. C. Williams, D. Wright, T. Yamada, H. Yoshida, and D. Zschiesche, Nucl. Instrum. Methods Phys. Res. A **506**, 250 (2003).
[111] J. Allison, K. Amako, J. Apostolakis, P. Arce, M. Asai, T. Aso, E. Bagli, A. Bagulya, S. Banerjee, G. Barrand, B.R. Beck, A.G. Bogdanov, D. Brandt, J.M.C. Brown, H. Burkhardt, Ph. Canal, D. Cano-Ott, S. Chauvie, K. Cho, G.A.P. Cirrone, G. Cooperman, M.A. Cortés-Giraldo, G. Cosmo, G. Cuttone, G. Depaola, L. Desorgher, X. Dong, A. Dotti, V.D. Elvira, G. Folger, Z. Francis, A. Galoyan, L. Garnier, M. Gayer, K.L. Genser,

V.M. Grichine, S. Guatelli, P. Guèye, P. Gumplinger, A.S. Howard, I. Hřivnáčová, S. Hwang, S. Incerti, A. Ivanchenko, V.N. Ivanchenko, F.W. Jones, S.Y. Jun, P. Kaitaniemi, N. Karakatsanis, M. Karamitros, M. Kelsey, A. Kimura, T. Koi, H. Kurashige, A. Lechner, S.B. Lee, F. Longo, M. Maire, D. Mancusi, A. Mantero, E. Mendoza, B. Morgan, K. Murakami, T. Nikitina, L. Pandola, P. Paprocki, J. Perl, I. Petrović, M.G. Pia, W. Pokorski, J.M. Quesada, M. Raine, M.A. Reis, A. Ribon, A. Ristić Fira, F. Romano, G. Russo, G. Santin, T. Sasaki, D. Sawkey, J.I. Shin, I.I. Strakovsky, A. Taborda, S. Tanaka, B. Tomé, T. Toshito, H.N. Tran, P.R. Truscott, L. Urban, V. Uzhinsky, J.M. Verbeke, M. Verderi, B.L. Wendt, H. Wenzel, D.H. Wright, D.M. Wright, T. Yamashita, J. Yarba, H. Yoshida, Nucl. Instrum. Methods Phys. Res. A **835**, 186 (2016).

[112] Glenn F. Knoll, *Radiation Detection and Measurement*, John Wiley & Sons (2010).

[113] M. J. Martin, Nucl. Data Sheets **114**, 1497 (2013).

[114] B. E. Glassman, D. Pérez-Loureiro, C. Wrede, J. Allen, D. W. Bardayan, M. B. Bennett, K. A. Chipps, M. Febbraro, M. Friedman, C. Fry, M. R. Hall, O. Hall, S. N. Liddick, P. O'Malley, W. -J. Ong, S. D. Pain, S. B. Schwartz, P. Shidling, H. Sims, L. J. Sun, P. Thompson, and H. Zhang, Phys. Rev. C **99**, 065801 (2019).

[115] Gordon R. Gilmore, *Practical Gamma-ray Spectroscopy*, John Wiley & Sons (2008).

[116] T. Palazzo, A. J. Mitchell, G. J. Lane, A. E. Stuchbery, B. A. Brown, M. W. Reed, A. Akber, B. J. Coombes, J. T. H. Dowie, T. K. Eriksen, M. S. M. Gerathy, T. Kibédi, T. Tornyi, and M. O. de Vries, Phys. Rev. Lett. **130**, 122503 (2023).

[117] Erik Jensen, Ph.D. Thesis, Aarhus University, Aarhus, Denmark, 2024.

[118] R. Mahajan, T. Wheeler, E. Pollacco, C. Wrede, A. Adams, H. Alvarez-Pol, A. Andalib, A. Anthony, Y. Ayyad, D. Bazin, T. Budner, M. Cortesi, J. Dopfer, M. Friedman, A. Jaros, D. Pérez-Loureiro, B. Mehl, R. De Oliveira, L. J. Sun, and J. Surbrook, Phys. Rev. C **110**, 08580x (2024).

[119] FRIB Decay Station White Paper.

[120] Y.A. Akovali, Nucl. Data Sheets **84**, 1 (1998).

[121] Mono. BIPM-5 - Table of Radionuclides, Vol.9 (to be published).

[122] Canberra Model 1407P Pulse Pair Generator.

[123] Marcell P. Takács, Karsten Kossert, Appl. Radiat. Isot. **176**, 109858 (2021).

[124] Chavdar Dutsov, Benoît Sabot, Philippe Cassette, Krasimir Mitev, Appl. Radiat. Isot. **176**, 109845 (2021).

[125] M. Honma, T. Otsuka, B. A. Brown, and T. Mizusaki, Phys. Rev. C **69**, 034335 (2004).

[126] B. A. Brown and W. D. M. Rae, Nucl. Data Sheets **120**, 115 (2014).

[127] A. Adams, C. Wrede, B. A. Brown, R. Longland, L. J. Sun, J. Dopfer *et al.*, in preparation.

[128] R. Longland, C. Iliadis, A. E. Champagne, J. R. Newton, C. Ugalde, A. Coc, and R. Fitzgerald, Nucl. Phys. A **841**, 1 (2010).

[129] C. Iliadis, R. Longland, A. E. Champagne, A. Coc, and R. Fitzgerald, Nucl. Phys. A **841**, 31 (2010).

[130] C. Iliadis, R. Longland, A. E. Champagne, and A. Coc, Nucl. Phys. A **841**, 251 (2010).

[131] P. Mohr, R. Longland, and C. Iliadis, Phys. Rev. C **90**, 065806 (2014).

[132] C. Iliadis, R. Longland, A. Coc, F. X. Timmes, and A. E. Champagne, J. Phys. G: Nucl. Part. Phys. **42**, 034007 (2015).

[133] K. Hämäläinen, S. Manninen, P. Suortti, S. P. Collins, M. J. Cooper, and D. Laundy, J. Phys.: Condens. Matter **1**, 5955 (1989).

[134] Ning Lu, Yi Hua Lam, Alexander Heger, Zi Xin Liu, and Hidetoshi Yamaguchi, arXiv:2406.14624.